The role of density currents and gravity waves in the offshore propagation of convection over Sumatra

Simon C. Peatman,[a] Cathryn E. Birch,[a] Juliane Schwendike,[a] John H. Marsham,[a] Chris Dearden,[b] * Stuart Webster,[c] Ryan R. Neely III[a,d] and Adrian J. Matthews[e]

[a] *Institute for Climate and Atmospheric Science, School of Earth and Environment, University of Leeds, Leeds, UK*

[b] *Centre for Environmental Modelling And Computation, University of Leeds, Leeds, UK*

[c] *Met Office, Exeter, UK*

[d] *National Centre for Atmospheric Science, Leeds, UK*

[e] *Centre for Ocean and Atmospheric Sciences, School of Environmental Sciences and School of Mathematics, University of East Anglia, Norwich, UK*

Corresponding author: Simon C. Peatman, Institute for Climate and Atmospheric Science, School of Earth and Environment, University of Leeds, Leeds, LS2 9JT, UK; s.c.peatman@leeds.ac.uk

*Current affiliation: The Hartree Centre, STFC Laboratory, Sci-Tech Daresbury, Warrington, WA4 4AD

ABSTRACT: The Maritime Continent experiences some of the world's most severe convective rainfall, with an intense diurnal cycle. A key feature is offshore propagation of convection overnight, having peaked over land during the evening. Existing hypotheses suggest this propagation is due to the nocturnal land breeze and environmental wind causing low-level convergence; and/or gravity waves triggering convection as they propagate. We use a convection-permitting configuration of the Met Office Unified Model over Sumatra to test these hypotheses, verifying against observations from the Japanese Years of the Maritime Continent field campaign. In selected case studies there is an organized squall line propagating with the land breeze density current, possibly reinforced by convective cold pools, at ~3 m s^{-1} to around 150–300 km offshore. Propagation at these speeds is also seen in a composite mean diurnal cycle. The density current is verified by observations, with offshore low-level wind and virtual potential temperature showing a rapid decrease consistent with a density current front, accompanied by rainfall. Gravity waves are identified in the model with a typical phase speed of 16 m s^{-1}. They trigger isolated cells of convection, usually further offshore and with much weaker precipitation than the squall line. Occasionally, the isolated convection may deepen and the rainfall intensify, if the gravity wave interacts with a substantial pre-existing perturbation such as shallow cloud. The localized convection triggered by gravity waves does not generally propagate at the wave's own speed, but this phenomenon may appear as propagation along a wave trajectory in a composite that averages over many days of the diurnal cycle.

SIGNIFICANCE STATEMENT: The intense convection experienced by the Maritime Continent causes high-impact weather in the form of heavy precipitation, which can trigger floods and landslides, endangering human life and infrastructure. The geography of the region, with many islands with complex coastlines and orography, means that the spatial and temporal distributions of convection are difficult to predict. This presents challenges for operational forecasters in the region; and introduces biases in weather and climate models, which may propagate globally. A key feature of the convection is its diurnal cycle and associated propagation offshore overnight from the islands. Although this phenomenon has been often investigated, there is no strong consensus in the literature on the mechanism or combination of mechanisms responsible. Improving our knowledge of these mechanisms and how they are represented in a convection-permitting model will assist forecasters to understand how and when the propagation of intense convective storms occurs, and allow model developers to improve biases in numerical weather prediction and climate models.

1. Introduction

The Maritime Continent (Ramage 1968) is the south-east Asian archipelago located in the oceanic warm pool between the equatorial Indian and Pacific Oceans. The equatorial location, warm sea surface temperature (SST) and presence of thousands of islands – where onshore sea breezes, driven by the diurnal land-sea temperature contrast, cause strong low-level moisture flux convergence – gives rise to some of the most intense convective storms on Earth. The associated latent heat release is so large that errors in simulating the spatial and temporal distributions of convection cause considerable errors in models on larger scales. These biases in convection over the Maritime Continent can lead to global biases, through processes such as Rossby wave propagation (e.g., Jin and Hoskins 1995).

The greatest form of variability in Maritime Continent convection is the diurnal cycle, with convection tending to peak over islands during the afternoon and evening, while the smaller-amplitude diurnal cycle over the sea has its peak in the early morning. Of specific interest in this study is the offshore propagation of convection overnight (e.g., Wu et al. 2009; Marzuki et al. 2022). This propagation is a crucial aspect of the distribution of convection, with Coppin et al. (2020) finding that 80% of all Maritime Continent rainfall is “coastal” – that is, it falls in a precipitation feature which intersects the coast. Peatman et al. (2021) showed how the nature

of offshore propagation depends on large-scale phenomena; here we investigate the causes of the propagation at a physical process level.

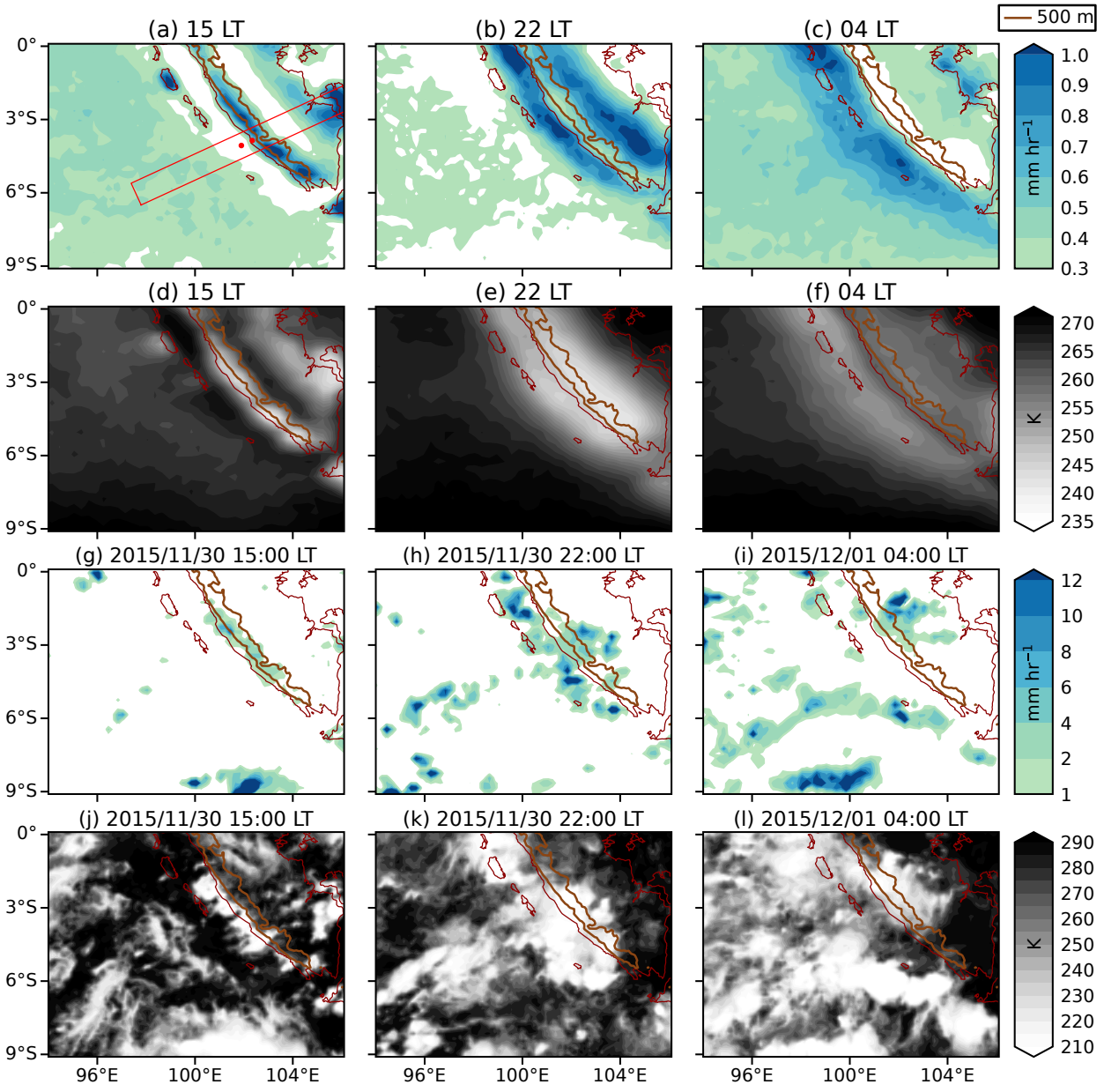

FIG. 1: (a–c) Composite diurnal cycle of observed precipitation rate over south Sumatra, from IMERG for November–April 2000/01–2020/21, showing selected times of day only. (d–f) As (a–c) but for observed 10.4 μm brightness temperature from the Himawari-8 satellite (channel 13) for November–April 2015/16–2019/20. (g–i) Observed precipitation rate for the same times of day as in (a–c) but for the 2015/11/30 case study. (j–l) As (g–i) but for observed 10.4 μm brightness temperature. Data are shown in local time (LT; defined as UTC+7). The Barisan mountains are shown by the 500 m orography contour (brown) from GLOBE. In panel (a) the red dots are the locations of the *R/V* Mirai during the 2015 field campaign and the town of Bengkulu; and the red box is used as the transect in figures 2 and 5.

The offshore propagation can be seen south-west of the island of Sumatra in figure 1. A composite mean of the observed diurnal cycle for boreal winter (November to April) is shown for selected times of day in figures 1a–c (precipitation rate) and 1d–f (brightness temperature, a proxy for convection as it shows the location of cloud tops, although brightness temperature picks out non-precipitating cirrus anvils so the relationship with precipitation is approximate). Over Sumatra, convective rainfall tends to form over the Barisan mountains (near the coast, indicated by the brown contour) during the afternoon. By late evening (figures 1b,e), the precipitation (although not the cloud tops at this time) is on average suppressed over the mountain ridge, but has begun to migrate both north-east and south-west. By early morning (figures 1c,f), there is rarely any precipitation over the mountains, with the most intense rainfall and cloud occurring offshore.

Of course, a composite as shown here suggests very smooth fields and the reader may be led to imagine a consistent behaviour in the timing and location of the convection day-to-day. In fact, observations of individual cases show spatially noisy rainfall (figures 1g–i) and cloud (figures 1j–l), much less coherent than implied by the composite even though this case has fairly strong propagation, beginning on 2015/11/30 and continuing overnight to 2015/12/01. This case study will be used throughout this paper.

Figure 2a shows a Hovmöller diagram of precipitation rate, for all times of day (with eight hours repeated to show the whole of the propagating signal), for the same composite as in figures 1a–c. In this composite the speed of the offshore propagation varies such that the envelope of precipitation widens as it propagates, with the slow edge at around 2 m s^{-1} and the fast edge over 13 m s^{-1}. The most intense rainfall occurs around 50–110 km offshore at 01 local time (LT; defined here as UTC+7), implying a propagation speed of around 3 m s^{-1} from the coast.

The range of speeds in the composite may be due to multiple modes of propagation being present on any given day (e.g., Vincent and Lane 2016, 2017; Yokoi et al. 2017; Coppin and Bellon 2019a); or because the modes of propagation themselves can vary in speed from day to day. Another possible cause is the inclusion of days with no propagation in the composite, so other convection offshore may contribute to the averaging without being associated with propagation. However, if we select only those days when the propagation occurs, using the method described in the appendix, the composite precipitation intensifies but the widening of the envelope is still apparent (figure 2b).

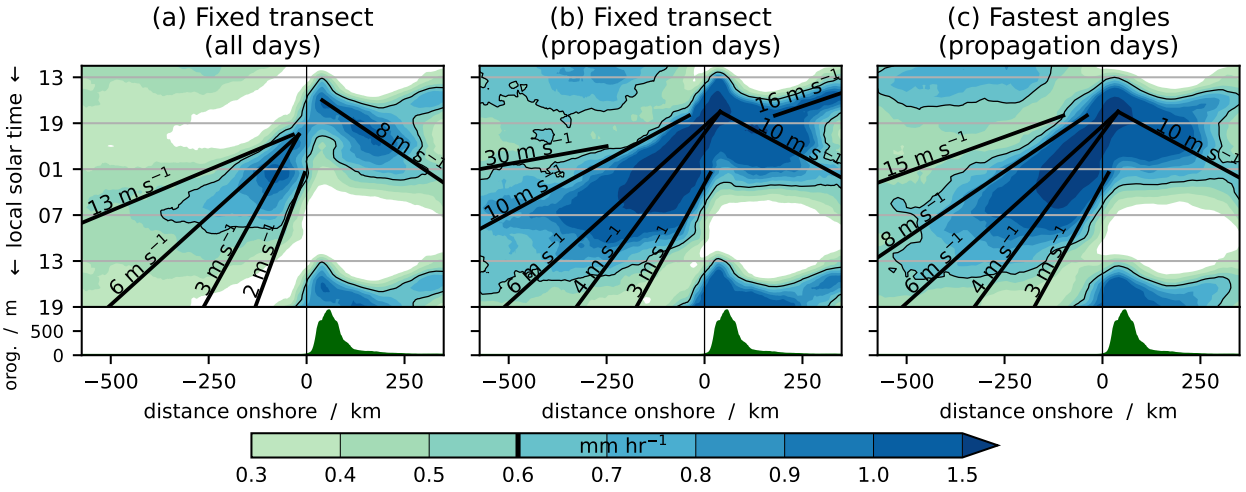

FIG. 2: (a) Onshore/offshore Hovmöller diagram of the composite diurnal cycle of observed precipitation rate also used in figures 1a–c, averaged over the red box in figure 1a. The 0.6 mm hr^{-1} contour is highlighted in black. Orography, averaged over the same box, is shown in green beneath the main plot. (b) As panel (a) but only for days when offshore propagation is diagnosed. (c) As panel (b) but using a variable transect, oriented in the direction of the propagation on each day. More details for (b) and (c) may be found in section 2c and the appendix. Propagation lines at selected phase speeds are overplotted in black.

Another possibility is that the direction of propagation varies between days, dependent on the environmental wind, so the apparent speed as projected onto the fixed box in figure 1a may not be the true speed. The impact of the varying direction of propagation is demonstrated by figure 2c, in which the transect for the Hovmöller diagram is not fixed, but is allowed to rotate about 102.05°E, 3.55°S. For each day with propagation, an angle is chosen to maximize the propagation speed; the algorithm for selecting this angle is also explained in the appendix. The propagation envelope still widens with distance from the coast, but it is less pronounced than in figure 2b. This widening implies there is variability in propagation direction and it does contribute to the shape of the composite propagation envelope, but even when this variability in direction is taken into account there is still a range of speeds present. Hence, there is a genuine variability in propagation speeds.

Many studies have investigated the physical processes involved in the offshore propagation over Sumatra and elsewhere, with a variety of mechanisms proposed but no clear consensus. Houze et al. (1981) found a regular diurnal cycle of rainfall over north Borneo and argued that the nocturnal offshore part of the cycle consisted of successive cloud clusters triggered due to low-level convergence between the land breeze from the coast and the boreal winter monsoon flow. However, studying offshore propagation over the Panama Bight, Mapes et al. (2003b,a)

argued against a similar mechanism due to the land breeze being too weak. They attributed the propagation to gravity waves forced by the heat source of the diurnal mixed layer. Many other studies since have also attributed the offshore propagation of convection to either gravity wave processes; or low-level convergence due to the land breeze or other density currents impinging on the environmental winds; or both. These mechanisms are discussed in the remainder of this section.

Evidence for propagation due to convergence caused by the land breeze was presented by Hassim et al. (2016) in a modelling study over New Guinea, and by Coppin and Bellon (2019a) in an idealized modelling study of a generic island in the tropics. However, cold pools from the diurnal convection can also cause density currents, and these similarly can lead to low-level convergence and trigger a propagating convection signal (Mori et al. 2004; Wu et al. 2009; Dipankar et al. 2019). Moreover, several papers have indicated that the presence of orography, such as the Barisan mountains close to the Sumatra coast, can cause or at least strengthen the boundary layer density currents that converge with the environmental wind, for example due to downslope winds which continue to propagate over the sea (Wu et al. 2009; Qian et al. 2012; Coppin and Bellon 2019b).

However, perhaps the most commonly cited mechanisms for the propagation are related to gravity waves (e.g., Love et al. 2011; Hassim et al. 2016; Yokoi et al. 2017; Coppin and Bellon 2019a), either due to direct triggering of convection by the wave or due to the wave destabilizing the atmosphere ahead of the convection. However, in the latter case it is not necessarily clear what controls the speed of the propagation behind the wave; and the gravity wave preconditioning also occurs on days without propagation of convection, so is not alone a sufficient condition (Yokoi et al. 2019).

Love et al. (2011) performed empirical orthogonal function analysis of vertical profiles of heating in a model simulation over Sumatra to identity gravity wave modes, tracking the wave propagation using the principal components. In a model simulation with convective parametrization on a 40 km grid, gravity waves were found at speeds of 60 m s^{-1} and 31 m s^{-1}. Because this is considerably faster than the propagation of convection, it was assumed that the waves precondition the atmosphere for the convection through increasing instability. In a simulation with explicit convection on a 4 km grid, the signals were diagnosed as having speeds of 40 m s^{-1} and 3 m s^{-1}, the latter being around

the same as the speed of the propagation of convection, but much slower than observed gravity waves.

Yokoi et al. (2017) analysed radiosondes from the *R/V* Mirai stationed offshore of Sumatra during a Years of the Maritime Continent (YMC; Yoneyama and Zhang 2020) field campaign (the "pre-YMC" campaign) run by the Japan Agency for Marine-Earth Science and Technology (JAMSTEC) in 2015. In a composite diurnal cycle of vertical profiles, a cooling and moistening of the air just above the boundary layer was found in the evening. This was hypothesized to be due to vertical advection caused by a gravity wave, with analysis showing that variations in potential temperature and humidity at this time and location are approximately consistent with vertical motion. However, from radiosondes alone it is not easy to confirm that gravity waves are responsible for these motions.

In an idealized study, Coppin and Bellon (2019a) argued that a gravity wave with a speed of 30 m s^{-1} was responsible for offshore propagation of convection although, in a composite diurnal cycle Hovmöller diagram, the correspondence between precipitation and a gravity wave trajectory is difficult to recognize (see their figure 4b).

Recently, studies have drawn a distinction between the physical mechanisms close to and far from the coast, consistent with figure 2. Vincent and Lane (2016) noted a slower propagation speed (3–5 m s^{-1}) 100–200 km from the coast and a faster speed (~18 m s^{-1}) further offshore. Bai et al. (2021) argued that the land breeze converging with low-level background westerly winds was responsible for slow (4.5 m s^{-1}) propagation within 180 km of the Sumatran coast, the range of the radar data they analyzed, although the speed of rainfall propagation as observed by the radar was typically slower than the propagation of the low-level convergence in a reanalysis. They also suggested that the role of gravity waves may dominate further from the shore. A survey of the global tropics, in addition to some extra-tropical locations, by Fang and Du (2022) also suggested that propagation observed near to coastlines may depend on density current propagation.

Despite the considerable volume of literature on the subject, therefore, a lack of consensus warrants further investigation. Here, we test the hypotheses that the offshore propagation of convection within the diurnal cycle of precipitation over Sumatra is caused by the nocturnal land breeze and/or gravity waves forced by land-based diurnal convection, over a range of distances from the shore. To do this, we perform a modelling investigation of case studies of offshore propagation

from Sumatra, verifying the results using observations from the automatic weather station (AWS) on the *R/V* Mirai during the pre-YMC field campaign (Yokoi et al. 2017). The model, and other data and methods, are described in section 2. Results are presented in section 3 and conclusions in section 4.

2. Model, data and methods

a. Convection-permitting MetUM forecasts

Reforecasts for 26 days of the JAMSTEC pre-YMC field campaign, from 2015/11/22 to 2015/12/17, were performed using the Met Office Unified Model (MetUM) version 11.1 at 0.02° (approximately 2.2 km) grid spacing, with explicit convection and 80 vertical levels. Previous work suggests that a fine horizontal resolution is necessary for research of this kind. Bhatt et al. (2016) found that, in a simulation over the Maritime Continent using the Weather Research and Forecasting (WRF) model with parametrized convection, a 10 km grid was not sufficient to capture all the local interactions between density currents. However, Birch et al. (2013) successfully captured the initiation of west African convective storms due to cold pools, using convection-permitting simulations on a 4 km grid.

The Regional Atmosphere v1 in the Tropics (RA1T) science configuration was used in our simulations (described in Bush et al. 2020 as RAL1-T). SST was fixed throughout each forecast using data from the Operational Sea surface Temperature and Ice Analysis (OSTIA). The domain is shown in figure 3 and the model was forced at the boundaries by the ECMWF global forecast initialized at the same date and time. Forecasts were initialized at 00 UTC daily from the ECMWF global 0.1° analysis, and the first 24 hours of each run were discarded to allow the model to spin up. Output from $T+24$ to $T+54$ (07 LT to 13 LT the following day) was analysed for each forecast. Diagnostics were output every 5 minutes.

Much of this paper focuses on a single forecast, initialized at 00 UTC on 2015/11/29. This is referred to as the 2015/11/30 case study.

b. Observations

Observations of precipitation are taken from the Global Precipitation Measurement (GPM) Integrated Multi-satellitE Retrievals for GPM (IMERG) product (Huffman et al. 2019). The

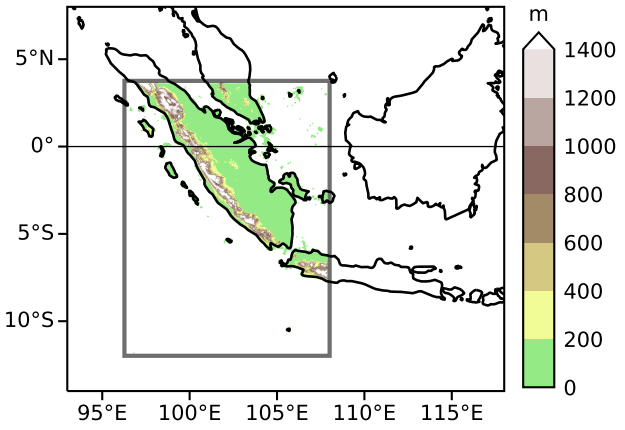

FIG. 3: Model orography for the convection-permitting MetUM experiment. The grey rectangle is the edge of the model domain and its thickness indicates the width of the lateral boundary forcing region.

IMERG algorithm merges precipitation estimates from microwave satellites, where available, and infra-red measurements, with calibration performed against data from a network of rain gauges. The data set is on a 0.1° grid at half-hourly temporal resolution.

During the pre-YMC field campaign, the *R/V* Mirai was stationed approximately 50 km offshore from the city of Bengkulu, on the south-west coast of Sumatra (red dots in figure 1a). An AWS recorded data every 10 minutes. In section 3c we use wind (measured at a height of 25 m); virtual potential temperature θ_v, which we compute from temperature and humidity (measured at 21 m); and precipitation rate.

Also on board the ship was a C-band polarimetric radar. We convert radar reflectivity Z in $\mathrm{mm}^6\ \mathrm{m}^{-3}$ to precipitation rate R in $\mathrm{mm\ hr}^{-1}$ using the Marshall-Palmer relation (Marshall and Palmer 1948)

$$Z = \alpha R^{\beta}, \tag{1}$$

where the parameters α and β were derived empirically by Yokoi et al. (2017) as $\alpha = 216$ and $\beta = 1.28$, using the method of Yokoi et al. (2012). Calibration was performed against a rain gauge at Bengkulu during 2015/11/23–2015/12/14 (i.e., the pre-YMC field campaign period, except during an active MJO event). The case studies examined in this paper fall within this time period.

Observations of brightness temperature are taken from the Himawari-8 geostationary satellite at 10.4 μm (Himawari channel 13). Images are available every 20 minutes. We transform the

full-disc images to a Cartesian grid with a grid spacing of 2 km, using the `gdalwarp` command from the Geospatial Data Abstraction Library (GDAL, 2022).

Orography is taken from the Global Land One-km Base Elevation (GLOBE) project (Hastings and Dunbar 1998; Hastings et al. 1999).

c. Methods

To investigate gravity wave activity in the model, we compute spectra in wavenumber-frequency space, as will be used in figure 9. A Hovmöller diagram of vertical velocity w, on a transect running along the direction of the nocturnal offshore propagation of convection, is taken at a selected vertical level. By analogy with Wheeler and Kiladis (1999), the fast Fourier transform (FFT) algorithm is applied in the x-dimension (onshore distance) and in time, to obtain complex coefficients in wavenumber k and frequency ω. Experiments showed that, although the w fields are not periodic in time or distance, the edge effects when computing the Fourier transforms are negligible. The modulus of these coefficients is computed. Following Peatman et al. (2018), a background spectrum, which is a function of ω, is found by averaging over k. We divide through by this background and plot $\log_{10}$ of the resulting field. For ease of interpretation, the k and ω axes are labelled with values of wavelength $|1/k|$ and period $1/\omega$, respectively.

The theoretical horizontal phase speed of a gravity wave of mode $n \in \mathbb{N}$ is (e.g., Lane and Reeder 2001)

$$\frac{\omega}{k} = \pm \frac{1}{n} \frac{N Z_T}{\pi}, \tag{2}$$

where Z_T is the tropopause height (taken to be 15.5 km) and N is the Brunt-Väisälä frequency, which we diagnose from the model. We overlay these theoretical speeds on the spectra in (k, ω) space, remembering the caveat that they are derived from dry theory so do not necessarily correspond exactly to the speeds of the waves that are present.

Gravity wave activity is further demonstrated (see figure 10) by high-pass filtering w to obtain w_{hp}. We use a Lanczos filter (Duchon 1979) with a cut-off frequency of $\omega_c = 1/(60 \text{ minutes})$ to remove low-frequency variability associated with deep convection, which develops on time scales of a few hours. Since gravity waves, according to theory, have the vertical profile of a standing wave with $n+1$ nodes, we use the tropospheric column average of $|w_{hp}|$ as a metric for gravity wave activity, the absolute value ensuring that even-numbered modes are not averaged out.

3. Results

a. Forecast verification and choice of case studies

We evaluate the performance of the forecasts first by comparing the mean precipitation rate over the entire 2015 field campaign period (figure 4). In IMERG observations (figure 4a), the precipitation during this time was strongly focused offshore to the south-west of Sumatra. Notably, this is in contrast to the November–April (NDJFMA) climatology in figures 1a–c, which has intense precipitation over the land also. The MetUM forecasts (figure 4b) more closely resemble the NDJFMA climatology, with intense precipitation over the mountains, especially in the southern half of the island. However, the model does have considerable precipitation offshore, as in the observations; and this is generally strongest in the south, again agreeing with IMERG.

Figure 4c shows the difference between the first two panels. There is mostly a positive bias over land as already discussed, on the order 0.5 mm hr^{-1}. Over the sea to the west of Sumatra, we find strong positive and negative biases. The spatial distribution of rainfall is not realistic on local scales, with the offshore precipitation being too intense around 4–5°S and too weak either side of this. However, the domain-average rainfall rate is a good match with observations, as the mean over the whole of figure 4c is close to zero (-0.07 mm hr^{-1}).

We further verify the model by considering the offshore propagation of precipitation south-west of Sumatra. Figures 5a and c show a Hovmöller diagram of observed precipitation rate with time running down the page. Overlaid in the black contour is the *R/V* Mirai radar (not available on 2015/11/22), interpolated onto the same fixed box as for IMERG except that it is limited in the onshore-offshore direction due to the radar's range. Where this range narrows, it is due to the motion of the ship away from its nominal station. The blue dashed lines show the locations of the *R/V* Mirai and Bengkulu. Figures 5b and d show the model precipitation rate from $T+24$ to $T+48$ (07 LT to 07 LT) for each forecast. Horizontally ruled lines are at 00 UTC (07 LT), where there are some discontinuities due to forecasts being concatenated together.

The forecasts are mostly successful at capturing which days are wet or dry, and usually manage to capture something of the offshore propagation. For example, on 2015/11/30 (see figures 1g–l for observations) the precipitation is initiated over the mountains at approximately the right time of day (in the afternoon), with propagation offshore which continues until the following morning.

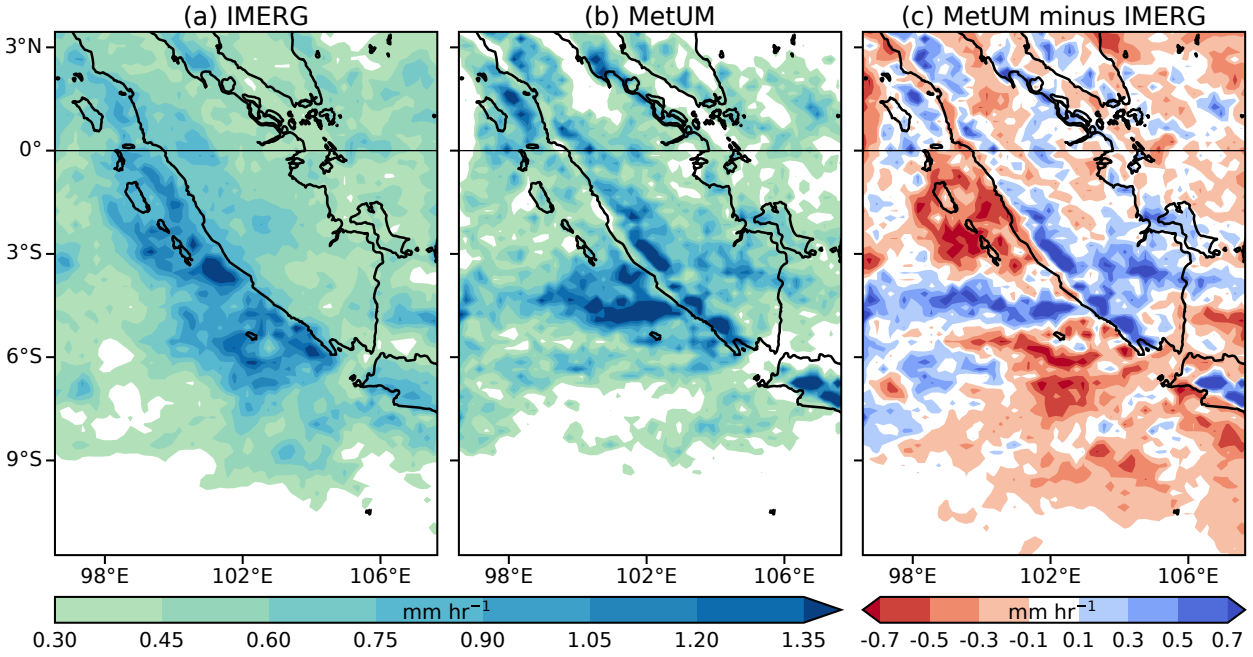

FIG. 4: (a) Observed precipitation rate from IMERG averaged over the 2015 field campaign (2015/11/22 to 2015/12/17). (b) As (a) but for the MetUM forecasts, regridded to the IMERG grid. (c) Bias in the MetUM (panel (b) minus panel (a)).

The propagation speed in the forecast is too slow, but it continues to around 99°E or beyond by 07 LT on 2015/12/01. (On 2015/12/01, the subsequent forecast correctly has more intense rainfall beyond 99°E.) Further examples of realistic propagation are on 2015/11/25, although the model has too much larger-scale rainfall offshore during the morning; and 2015/12/03, although the propagation is again a little too slow. From 2015/12/13, an active MJO event occurred (in phase 4, using the Realtime Multivariate MJO (RMM) indices of Wheeler and Hendon 2004), associated with relatively large-scale rainfall which tends to propagate onshore. The transition to this new pattern of propagation is also well forecast.[1] Days on which the forecasts do not verify so well against observations include 2015/12/07, when intense offshore precipitation throughout the day was observed; and 2015/12/10, which does not capture the intense land-based precipitation or its propagation, instead having intense rain over the sea.

For the remainder of this section we focus on three case studies, namely 2015/11/25, 2015/11/30 and 2015/12/03, all of which have offshore propagation in the observations which is well represented by the forecasts. As explained above, there are forecast biases for these three cases, but from this

[1]The daily mean rainfall in the Sumatra region on these days was low compared with most of the field campaign, which is unusual for an active MJO event. This is explained by a dry air intrusion from the extra-tropical southern hemisphere, which occurred concurrently.

point we are interested in these forecasts as research tools, to understand the physical mechanisms behind the offshore propagation of convection. Therefore, having established that the broad features of these case studies are correctly forecast, we are not concerned with smaller discrepancies from observations, which are typical of forecasts of convective activity.

Maps of precipitation rate are shown for each of these case studies for four selected times of day in figure 6, starting during the afternoon (15 LT) and evening (21 LT), and following the propagation through the early morning of the following day (01 LT and 05 LT). Overplotted maroon contours show the magnitude of the horizontal gradient of θ_v,

$$|\nabla_h \theta_v| \equiv \sqrt{\left(\frac{\partial \theta_v}{\partial x}\right)^2 + \left(\frac{\partial \theta_v}{\partial y}\right)^2},$$

at 45 m above sea level. This is plotted over sea only as it is a noisy field over land; and only the 0.1 K km^{-1} contour is shown. This indicates the presence of low-level fronts, which may be caused by either the land breeze converging with environmental onshore wind; or cold pools due to convection. In some places it is not easy to distinguish the two, but the orange shapes (drawn subjectively) approximately indicate the land breeze location, with possible reinforcement from cold pools. The red boxes, again drawn subjectively, follow the convection offshore and are used for subsequent Hovmöller diagrams and vertical cross-sections (figures 7–12).

In all three cases, precipitation forms over the mountains near the coast by 15 LT, with rain rates exceeding 15 mm hr^{-1} in places. By 01 LT, the main rainfall has propagated from the island to the coastal sea. Over land in the afternoon, precipitation is represented as a large number of small-scale and intense convective cells, while the offshore precipitation overnight is more organized, as a squall line. This squall line propagates away from the coast along with the land breeze front. Note that neither the squall line nor the land breeze front necessarily preserve the shape or orientation of the coastline. Instead, they may be curved (e.g., figure 6c) or split into multiple features (e.g., figures 6g–h), which may be due to factors such as the environmental wind or interactions with cold pools.

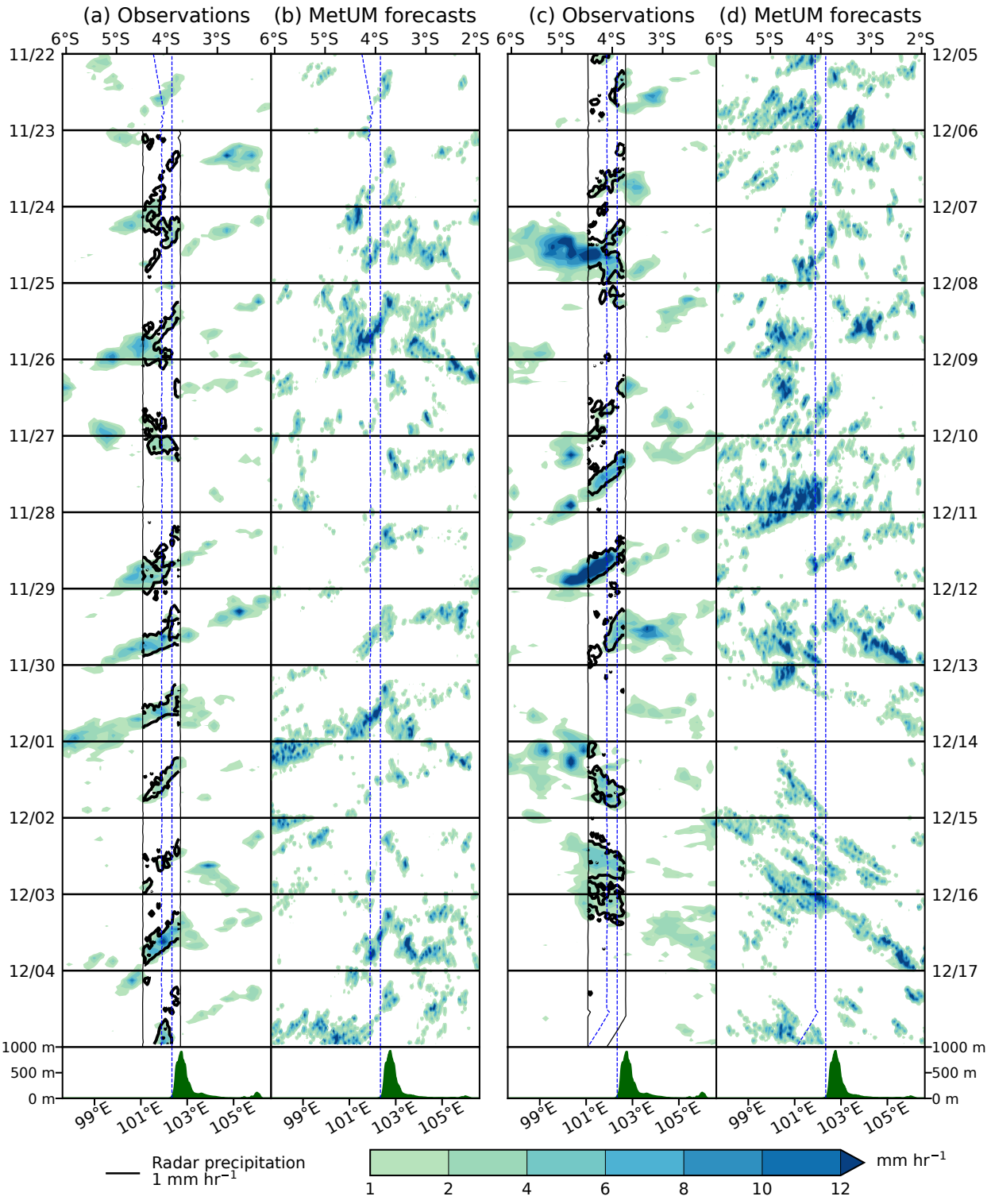

FIG. 5: Hovmöllers of precipitation rate during the 2015 field campaign taken along a transect passing through Bengkulu and the mean *R/V* Mirai position, averaged over a box of width 1°, from (a,c) GPM IMERG (shading) and the *R/V* Mirai radar (black contours); and (b,d) the MetUM forecasts. (a,c) Solid black vertical lines indicate the range of the radar transect. Dashed blue lines indicate the track of the *R/V* Mirai and the location of Bengkulu. Horizontal grid lines are at 00 UTC (07 LT); successive forecasts are concatenated at these times. Mean orography across the transect is shown in green below each panel.

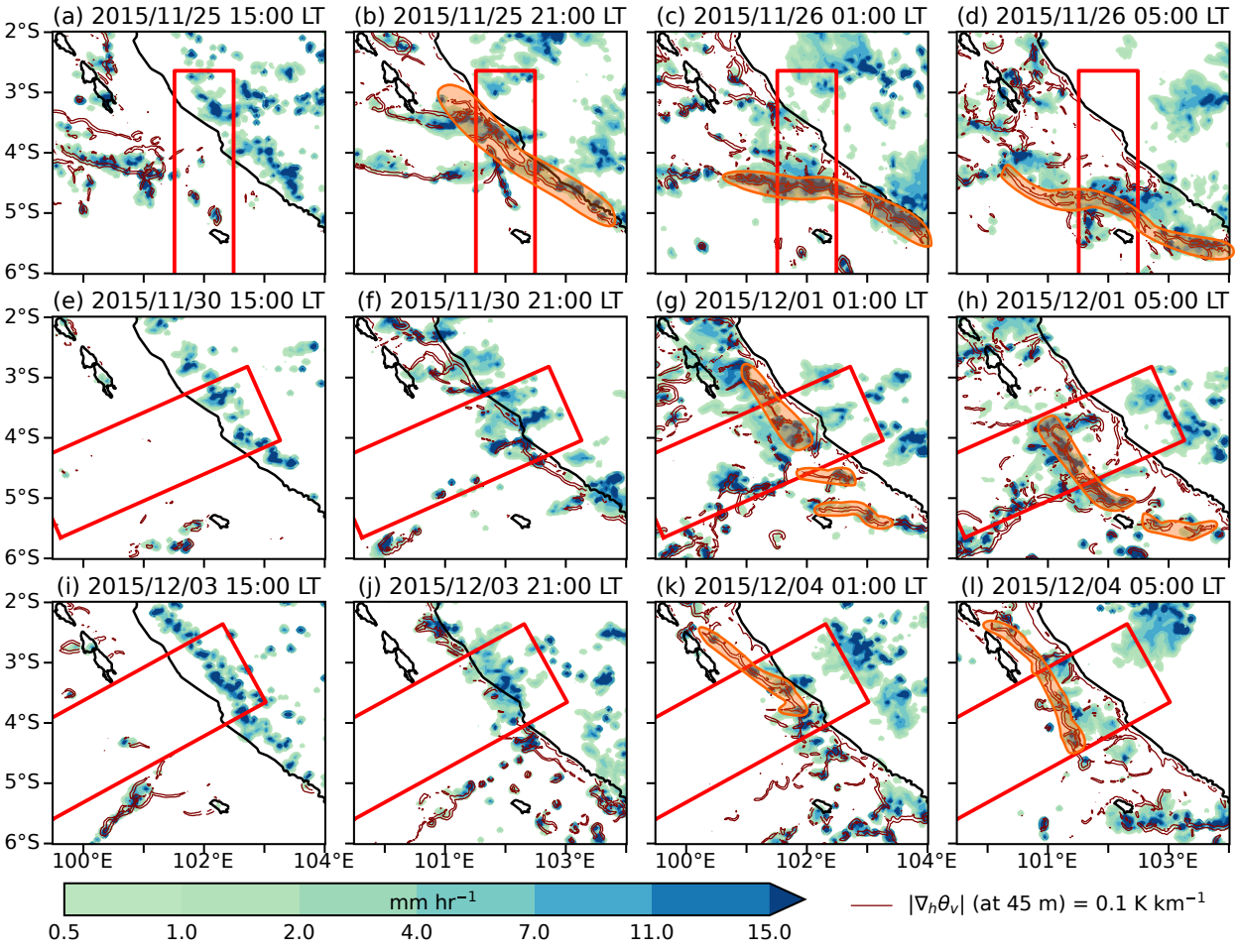

FIG. 6: Forecast precipitation rate at selected times from the (a) 2015/11/25, (b) 2015/11/30 and (c) 2015/12/03 case studies. The magnitude of $\nabla_h \theta_v$ at 45 m altitude is overplotted in maroon, over the sea only, to identify low-level fronts caused by the land breeze and cold pools. The approximate location of the land breeze front is indicated by the orange shapes. The red boxes are drawn subjectively to follow the propagation of convection and are the transects used for figures 7–12.

b. Mechanisms of offshore propagation

To investigate the physical mechanisms of the offshore propagation more closely, we consider vertical cross-sections of the 2015/11/30 case (figure 7). These are averaged over the red box in figures 6e–h, so the long edge of the box is the horizontal axes of the plots.

For this case study, the wind in the free troposphere blows offshore (coloured shading and vectors) throughout the day in almost all locations shown. Close to the ground, by local noon (figure 7a) there is an onshore sea breeze. This is driven by the land-sea temperature contrast, which peaks around this time at 6.3°C (not shown; taking the difference between the means up to 20 km either

side of the coast; but recall from section 2a that there is no diurnal cycle of SST in this model). The sea breeze results in upslope flow and, at the peak of the mountains, there is moisture flux convergence (MFC; red curve on lower panel). There are low- to-mid-level clouds (grey contours), probably cumulus, at a fairly low concentration directly above the mountain peaks, but they are not precipitating (blue curve on lower panel). The lack of rainfall is typical for this time of day.

By 16 LT (figure 7b), deep convection has been triggered over the mountain, forming cumulonimbus clouds with associated intense precipitation, varying from around 5 to 13 mm hr^{-1}. The sea breeze has intensified and extended further offshore. By 20 LT (figure 7c), the convection has deepened further, reaching the tropopause. As the land surface cools, a katabatic flow begins on the seaward side of the mountains, as seen by the blue shading (horizontal flow in the offshore direction) around 5–40 km inland and the lower-θ_v air (black contours). As a result, there is low-level convergence with the sea breeze just inland of the coast. The deep convection and high precipitation rate (10–16 mm hr^{-1}) are collocated with this convergence, rather than being centred near the mountain peaks.

Through the late evening and early morning (figures 7d–f), the density current initiated as the katabatic wind continues to flow downhill and offshore as a land breeze current. During these hours (22–03 LT), the land surface is cooler than the sea surface by about 4–5°C in the model. Air behind the cold front has θ_v in the range 301–303 K, whereas in the well-mixed boundary layer ahead of the front we typically have $\theta_v \sim 304$ K. The strongest ascent of air, low-level convergence and precipitation propagate along with the front, with the precipitation rate gradually weakening (13–22 mm hr^{-1} at 22 LT and 4–17 mm hr^{-1} at 03 LT). This is consistent with the mean diurnal cycle, in which precipitation has propagated beyond the coast by 22 LT (figure 1b), weakening as it propagates further through the night (figure 1c).

At a number of times and locations, gravity waves can be seen in the wind field. For example, alternating ascending and descending air is visible above around 9 km altitude across the domain in figures 7a and b; and around 3–6 km altitude at around 75 km and 125 km offshore in figure 7b. Note also the ascent around 1–3 km altitude at around 150 km offshore in figure 7c. Note further that there is convection and associated precipitation away from the land, not directly associated with the initial convection over the mountains, around 190 km offshore (figures 7d and e). Inspecting the maps of precipitation rate (figures 6f and g) reveals that this convection (around 101°E, 5°S) is

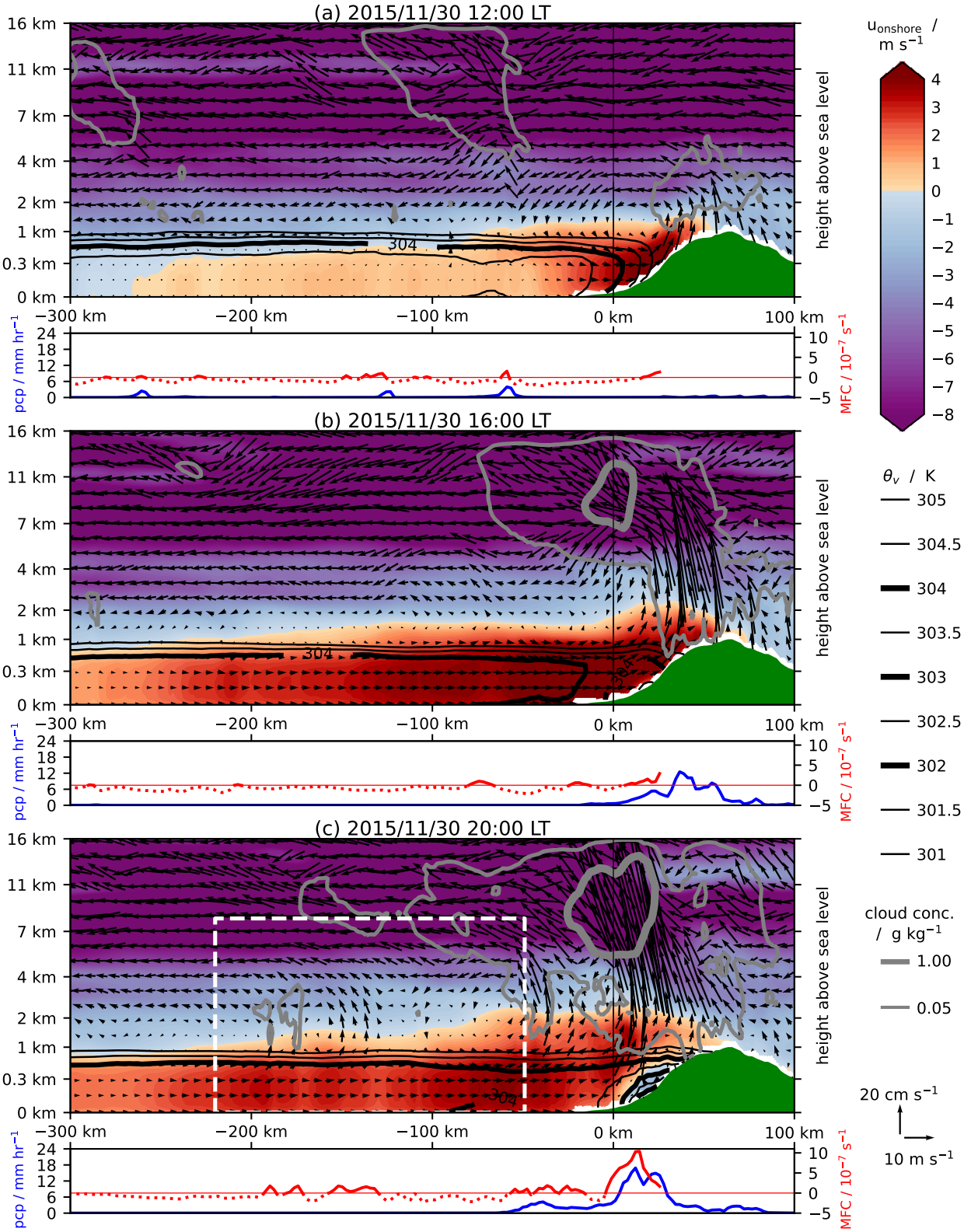

FIG. 7: Vertical cross-sections at selected times of the forecast of the 2015/11/30 case study, showing onshore and vertical wind (vectors, with onshore wind also in coloured shading); virtual potential temperature θ_v (black contours, shown up to 305 K only to illustrate the thermodynamics of the boundary layer, which is usually well-mixed); liquid+solid cloud concentration (grey contours); orography (green); precipitation rate (blue curve); and along-transect moisture flux convergence (MFC) averaged over 0–500 m above sea level (red curve; solid for convergence and dotted for divergence). The white dashed box in panel (c) is the domain of figure 11. The vertical axes of the main panels (height above sea level) are non-linear, to emphasize the lower troposphere.

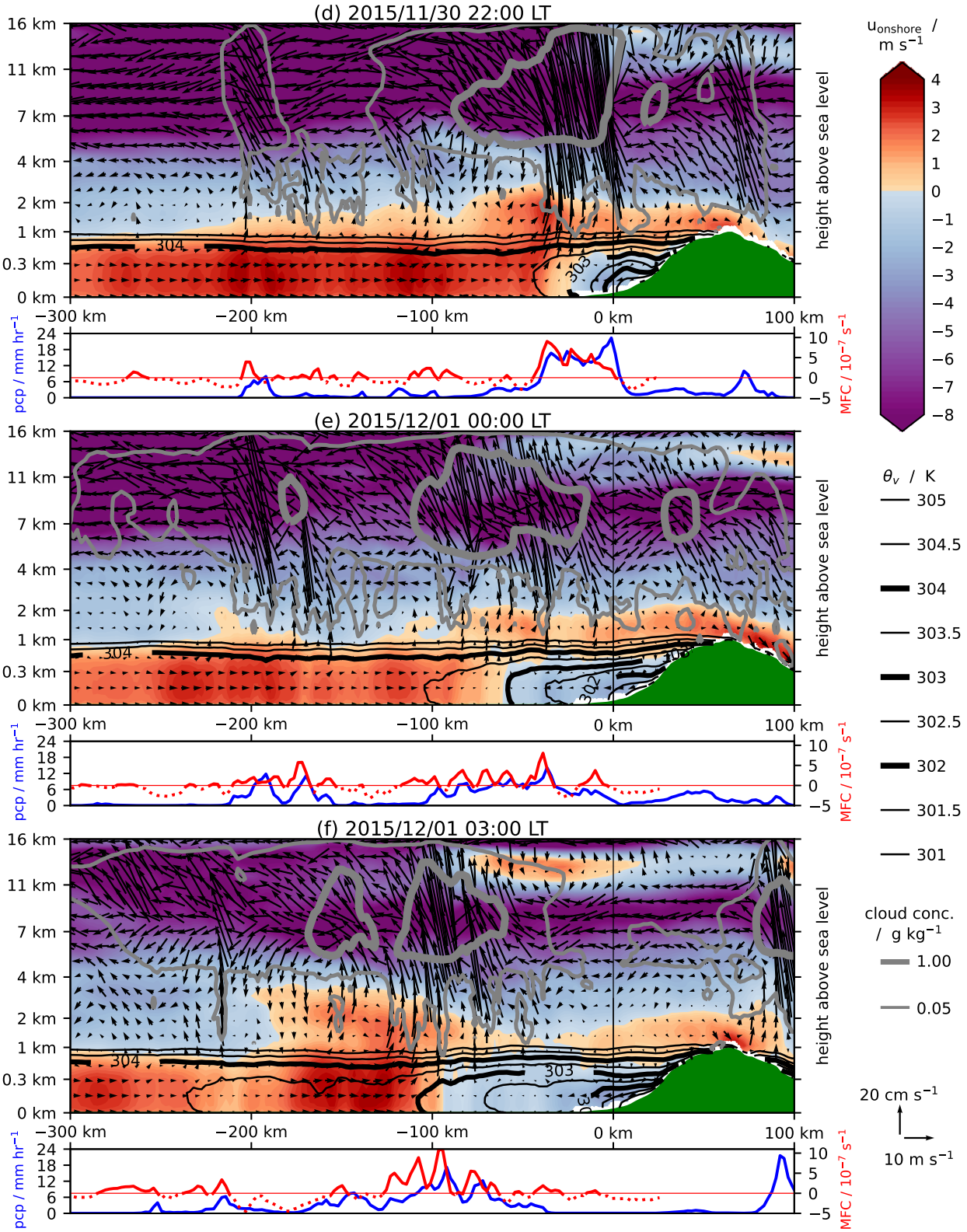

FIG. 7: Continued.

far more localized than that which propagates away from the coast with the land breeze, the latter being a large, organized squall line. The waves and offshore convection will be discussed in more detail later in this section.

Having examined the vertical cross-sections of one case study and seen that the propagating squall line follows the low-level convergence due to the land breeze front, we now demonstrate that this is common to all three of our case studies. Figures 8a–c show Hovmöller diagrams of the onshore component of 10 m wind. The red shading during the day is the sea breeze, with the land breeze in blue being initiated slightly inland over the mountains at around 16–18 LT. It propagates offshore at approximately 2.5–3.5 m s^{-1}. As seen in the vertical cross-sections of the 2015/11/30 case, in all three cases the precipitation propagates along with the land breeze front, sometimes with a lag of 1–2 hours between the change in wind direction and the heaviest rainfall. This may suggest the convection can take time to respond to the changing low-level wind; or it may be an indication of the convection forcing a cold pool in front of it as it advances.

Figures 7 and 8a–c have considered the onshore component of wind and convergence only. To confirm that the precipitation is synchronized with the total low-level horizontal convergence, we also show Hovmöller diagrams of the 10 m divergence in figures 8d–f. Again, we see the precipitation is synchronized with the convergence (blue shading).

The evidence, therefore, points towards a similar mechanism as that of Houze et al. (1981), with the convergence between the land breeze and the environmental winds being the chief driver of the nocturnal offshore propagation. However, given the numerous references to the role of gravity waves in the literature (see section 1), we now turn our attention to the gravity waves in the model to examine any role for them, using the 2015/11/30 case as an example.

Figure 9 shows wavenumber-frequency spectra, computed as described in section 2c, at (a) 2 km and (b) 13 km above sea level. At 13 km, the gravity wave activity is significant (i.e., distinguishable from the background spectrum, which has been removed) in the offshore direction across all frequencies up to the Nyquist frequency of $\omega_N = 1/(10 \text{ minutes})$. At 2 km the picture is very similar, but with less spectral power at the very highest frequencies. The absence of power in the onshore direction is likely due to the prevailing wind direction. The theoretical gravity wave phase speeds were computed using $N = 0.01014$ s^{-1}, a mean value diagnosed from the model. At both altitudes, there is power in the $n = 2$ (25.0 m s^{-1}), $n = 3$ (16.7 m s^{-1}) and $n = 4$ (12.5 m s^{-1}) modes.

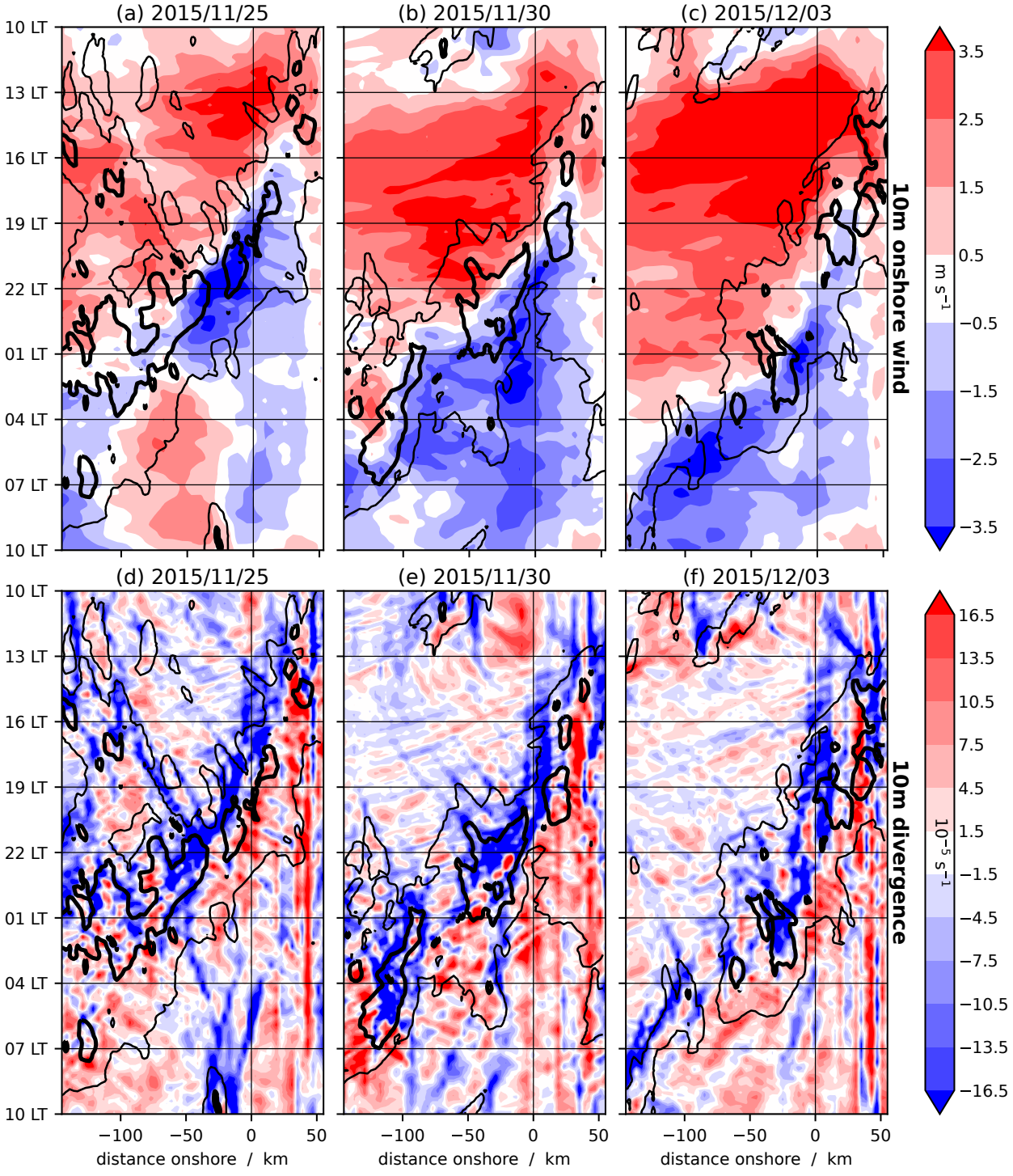

FIG. 8: Hovmöllers of 10 m (a–c) onshore wind and (d–f) horizontal divergence, with precipitation rate overlaid (contour levels: 1 and 10 mm hr^{-1}), for case studies on (a,d) 2015/11/25, (b,e) 2015/11/30 and (c,f) 2015/12/03.

It is perhaps surprising that the $n = 1$ (50.0 m s^{-1}) mode appears to be absent. However, we note that observed gravity waves propagate slightly more slowly than in the dry theory used to estimate theoretical speeds here; and the waves do not necessarily propagate in the same direction as the transect chosen in figures 6e–h, so it is possible they are diagnosed as propagating more slowly than their true speed, due to their projection onto the chosen onshore-offshore coordinate. The box is at an angle of about 45° to the equator, so in a fairly extreme case of the waves propagating due west or due south, the diagnosed speed would be a factor of cos 45° times the true speed. Hence, we can consider that the wave speeds may be as diagnosed or up to around 40% faster.

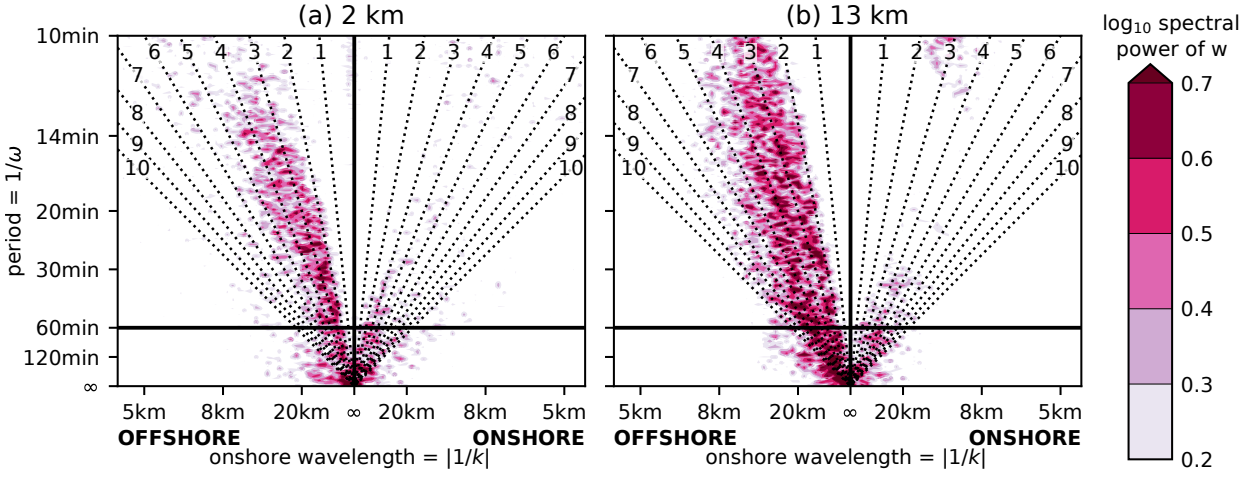

FIG. 9: Wavenumber-frequency spectra of w at (a) 2 km and (b) 13 km altitude, from a Hovmöller diagram of the 2015/11/30 case study forecast, with the background spectrum removed. Dashed lines are theoretical dispersion relations for gravity waves of modes $n \in \mathbb{N}$; see equation (2). A horizontal line is drawn at a period of 60 minutes, which is used as the cut-off frequency for the high-pass filter of w used in figures 10a, c and d.

Having demonstrated that spectra of w have power along the dispersion lines of gravity waves, we consider how their propagation relates to the occurrence of convection in the model. Figure 10b is a Hovmöller diagram of the column-mean (over the troposphere) of w for the 2015/11/30 case study. This, of course, most prominently shows the deep convection, in the brighter colours. We also see, in purple, small-scale features propagating at faster speeds. These are the gravity waves which were found in figure 9. To isolate these waves from the convection, we use a high-pass filter as described in section 2c (figure 10c). Precipitation rate and theoretical gravity wave speeds are overlaid. This is repeated for the other two case studies in figures 10a and d.

As expected from the wave spectra, the speeds of propagation are consistent with modes $n = 2$–4. The propagation of deep convection is much slower, at the speed of a theoretical wave of order $n = 10$ or even higher, which is much higher than typically observed, so it is not reasonable to suppose that this convection propagates as a direct result of gravity waves.

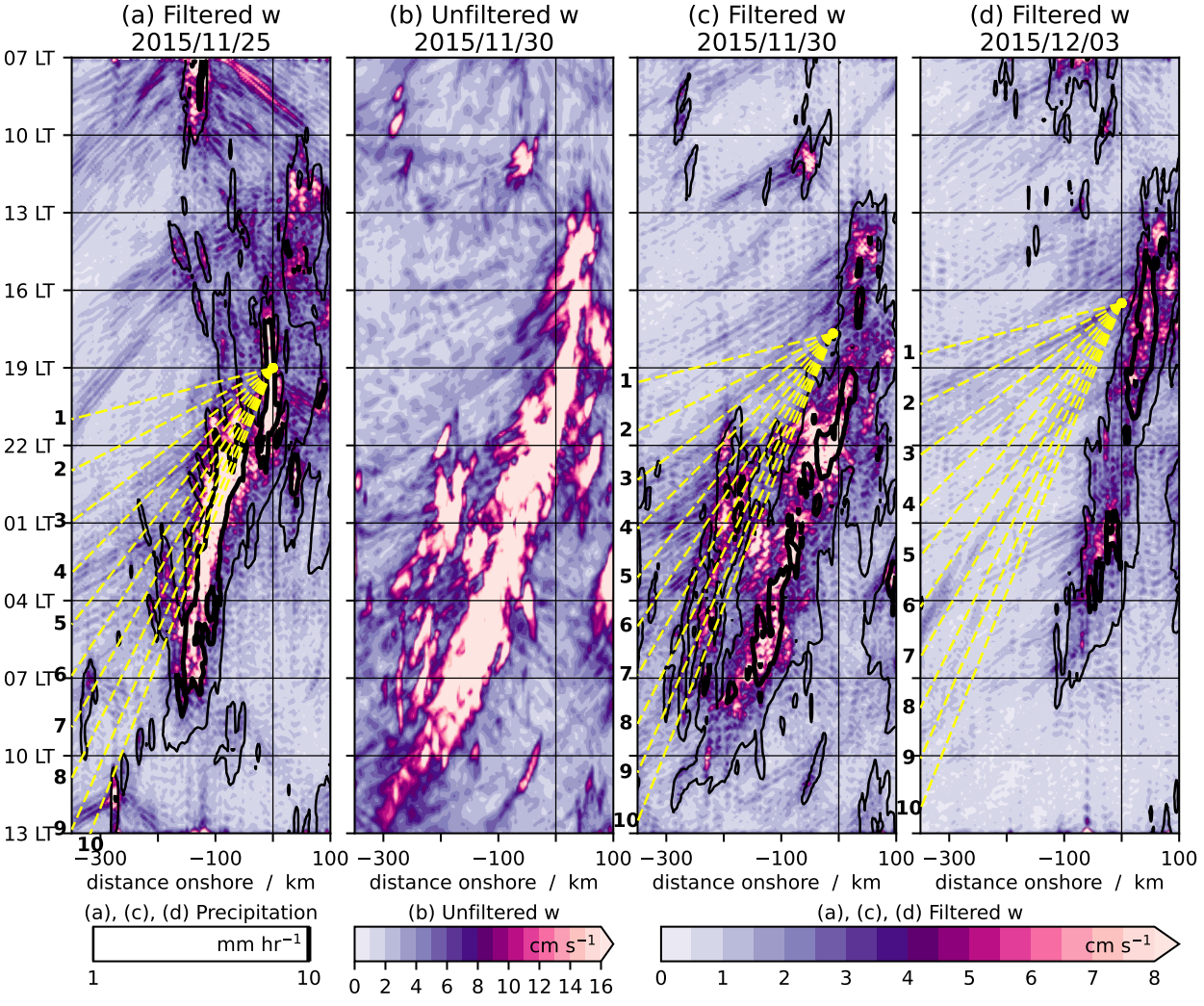

FIG. 10: (a,c,d) Hovmöller diagrams of column-mean absolute value of w_{hp} (frequency cut-off at 60 minutes, shown by the horizontal line in figure 9), with precipitation rate overlaid, for the 2015/11/25, 2015/11/30 and 2015/12/03 case studies, respectively. Also overlaid are theoretical gravity wave phase speeds, starting at a subjectively-chosen time and position (marked with a yellow dot), and labelled with their mode number n. (b) As (c) but for w, not w_{hp}.

However, there are some instances of precipitation occurring ahead of the main branch of propagating convection. Examples for 2015/11/25 (figure 10a) include −130 km at 22:15 LT, −145 km at 23:00 LT and −235 km at 00:00 LT; and for 2015/11/30 (figure 10c), −105 km at

20:25 LT and −175 km at 20:35 LT. Since these regions of precipitation occur well ahead of the land breeze, it is conceivable that they are associated with the gravity waves.

The latter example (−175 km in figure 10c) develops into the intense convection which was highlighted earlier in this section, occurring at around −190 km in figures 7d and e. In this instance, we can see the process of a gravity wave triggering the convection in vertical cross-sections. Figure 11 is a repetition of figure 7 but for the white dashed region in figure 7c only, between 19 LT and 21 LT. The ascending air highlighted with the green ellipse is a gravity wave (see the discussion of figure 12, below), propagating at around 16 m s^{-1}, which is close to the theoretical speed of an $n = 3$ wave. In this instance it happens that there is a small perturbation at around −190 km, in the form of a small region of non-precipitating cloud. This was caused by a cold pool (not shown) which propagated away from some other convection found offshore earlier in the day (which can be seen around 101–102°E, 5.5–6°S in figure 6e, outside the transect area). By 21 LT, figure 11d shows that the wave has reached this perturbation, strengthening the ascending air there and causing the cloud to precipitate. An hour later, the convection has reached the tropopause (figure 7d) and by midnight it has intensified into a major convective feature (figure 7e). The feature can be seen centred around −190 km in figure 10c.

We can satisfy ourselves that the propagating region of ascending air in figure 11 really is a gravity wave by studying figure 12. Here, we take Hovmöller diagrams of w (no longer filtered or vertically-averaged), at 2 km above sea level since this is where the feature was seen in the vertical cross-sections. In figure 12b we overlay contours of potential temperature θ. The yellow dashed-dotted line is the feature in question. We see that w and θ are in quadrature, as expected for a gravity wave. For example, at −125 km there is a maximum in θ at 19:25 LT, after the descending (blue) phase of the wave. This is consistent, as the descent has brought down higher-θ air from above. The maximum in w is at 19:45 LT, at which point θ is decreasing, which is again consistent as the ascent is bringing up lower-θ air from below.

The yellow stars in figure 12a are locations where ascent is triggered along the trajectory of the gravity wave propagation, followed by precipitation within around 15–20 minutes. In figure 12b we see that these ascent features do not propagate or have the same quarter-phase relationship with θ. Instead, the maximum in w coincides with a maximum in θ, consistent with diabatic heating due to convection. Since these instances of precipitation are mostly low-intensity, small-scale and isolated

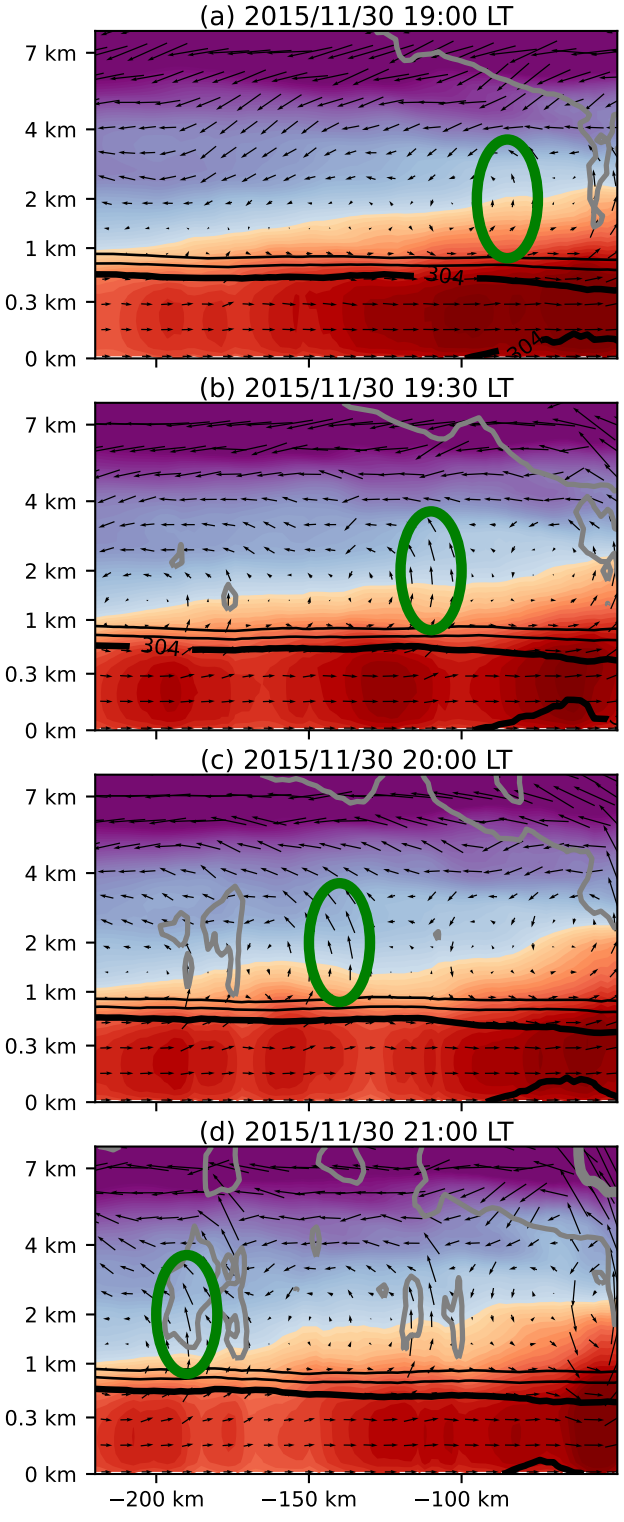

FIG. 11: As figure 7 but for a limited horizontal and vertical extent, as indicated by the white dashed box in figure 7c, and for different selected times. Green ellipses indicate the ascending phase of a particular gravity wave (see figure 12) propagating offshore. For a description of the plotted quantities, see the colour bars and caption of figure 7.

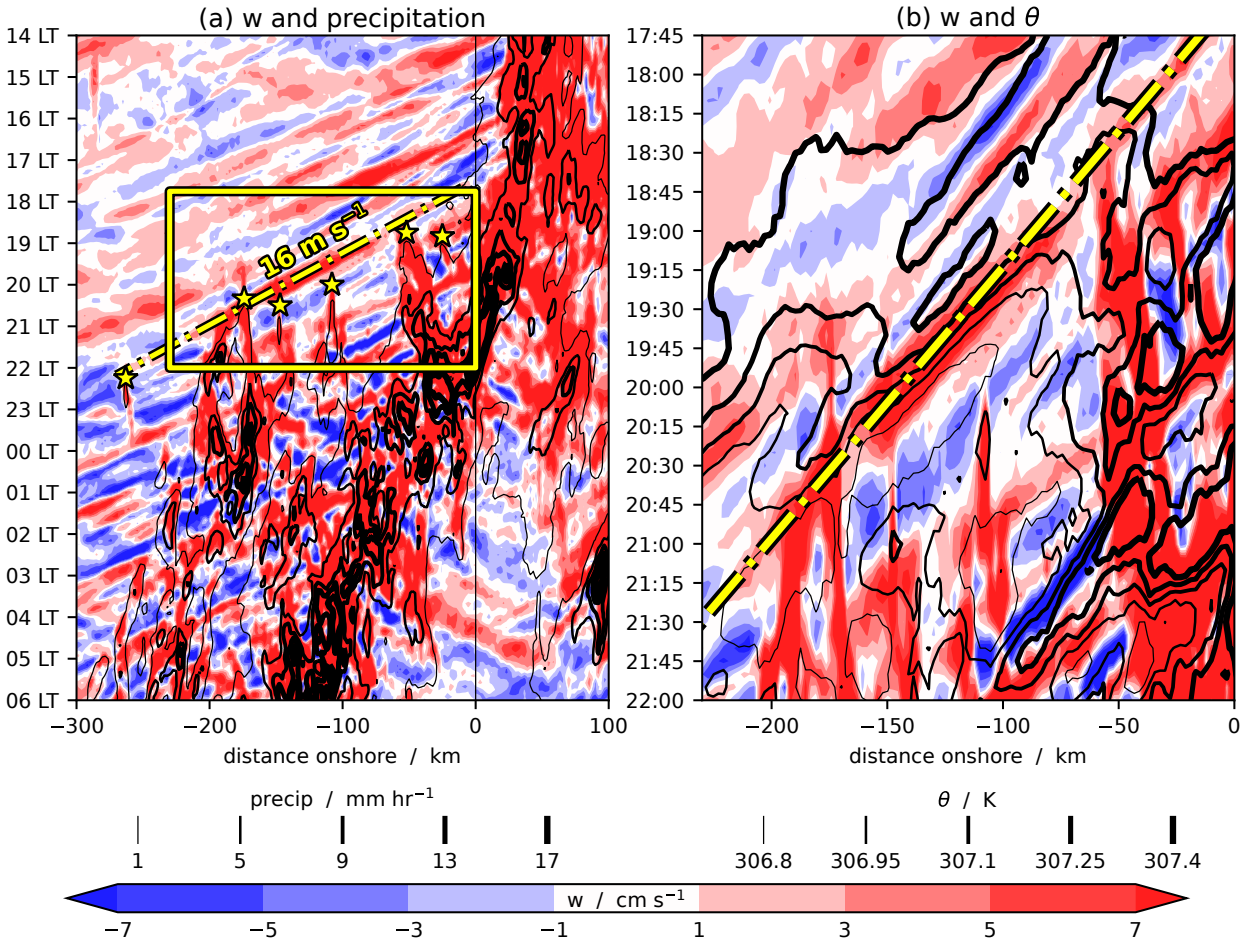

FIG. 12: Hovmöller diagrams of unfiltered vertical velocity w at 2 km altitude from the 2015/11/30 forecast case study (coloured shading). The yellow dashed-dotted line is the gravity wave indicated in figure 11. Black contours are (a) precipitation rate and (b) potential temperature θ at 2 km altitude. In panel (a), the six yellow stars indicate initiation of precipitation, likely triggered by the gravity wave; and the yellow box is the domain of panel (b).

(not organized), they cannot truly be considered propagation. However, when compositing over many days, such precipitation would be smoothed out in the averaging and appear as propagation. This explains the faster part of the widening propagating envelope that is seen in figure 2a.

c. Verification of physical mechanisms

The previous section proposed physical mechanisms of the offshore propagation, derived from an in-depth analysis of high-resolution model case studies. There are not many observations that can be used to verify these mechanisms, but the 2015 field campaign (see section 2b) provides us with point measurements from the *R/V* Mirai. In figures 13a–g we present time series of forecast

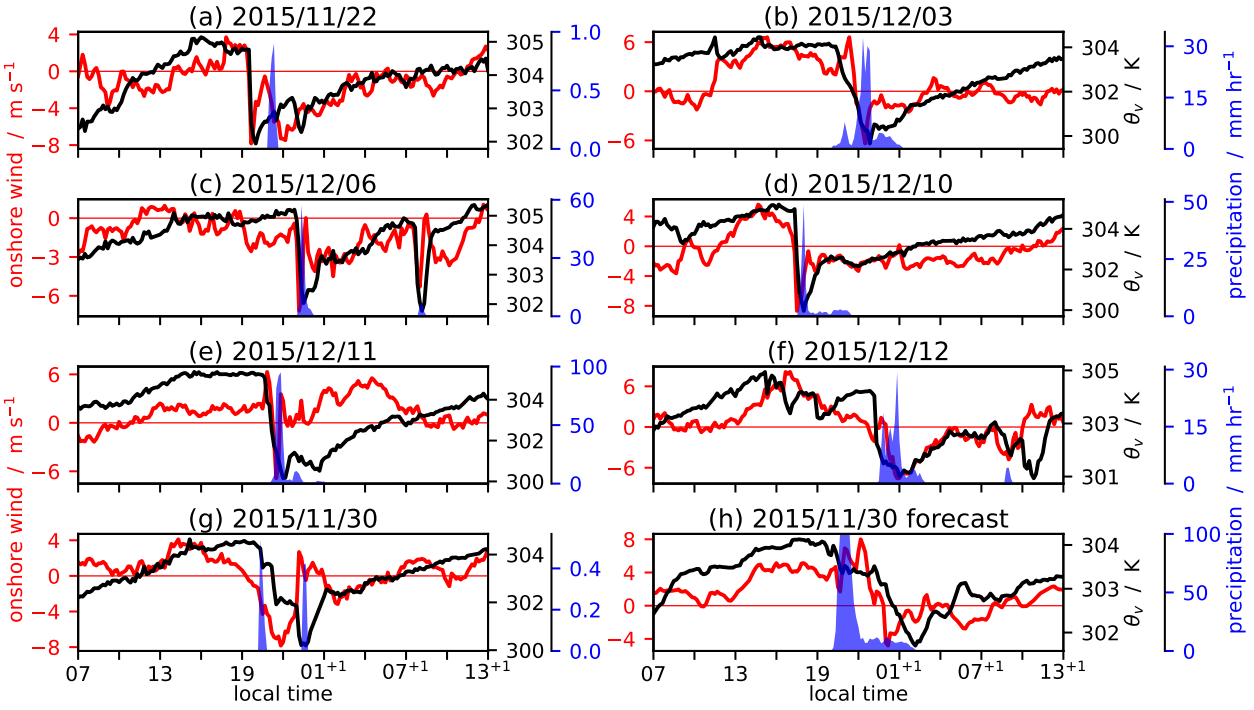

FIG. 13: (a–g) Time series from the *R/V* Mirai AWS on seven chosen dates. Curves are onshore wind (red) and θ_v (black), and filled blue region is precipitation rate. Local time is shown on the horizontal axis, with $^{+1}$ indicating the day after the date given in the panel title. Note that (g) is out of chronological order, for ease of comparison with (h) the 2015/11/30 case study from the forecasts.

onshore wind, θ_v and precipitation rate, for seven chosen dates. Figure 13h is the equivalent for the 2015/11/30 forecast, interpolated to the same location as the *R/V* Mirai, and with wind and θ_v interpolated to the same levels as recorded by the AWS.

The observed cases in figures 13a–f all show a density current passing over the *R/V* Mirai in the evening or overnight. The onshore component of the wind switches from positive (onshore) to negative (offshore), accompanied by a sharp decrease in θ_v of 2–3 K, typically in around 30–40 minutes. There are two candidates for these density currents – the land breeze and cold pools. It is very difficult to differentiate between the two, especially in observations, as they are in essence the same phenomenon, albeit with a different cause.

However, the land-sea temperature contrast driving an offshore-directed land breeze is well documented, so we expect the land breeze to be seen in these observations. At around 08 LT on 2015/12/07 (figure 13c; i.e., 08^{+1} LT for the 2015/12/06 case) there is a brief reduction in θ_v, along

with a shift to offshore winds and fairly light rain. This occurs around 9 hours after the probable land breeze feature, and may be a cold pool front passing over.

These frontal features are always either accompanied by or shortly followed by rainfall, which may be intense but does not fall over the *R/V* Mirai for long. This is consistent with the land breeze being responsible for rainfall propagating away from the land.

The variability in rainfall intensity is considerable. For the six cases chosen, the peak rainfall rate varies from around 0.9 mm hr^{-1} to around 95 mm hr^{-1}. However, precipitation rate can be highly spatially variable, so the large range of values may arise from the fact that we are considering precipitation at a single point only, so we are sampling from this highly variable field. Although the land breeze-driven propagating convection tends to take the form of a squall line, it does not necessarily follow that all precipitating parts of the system are contiguous.

For the 2015/11/30 case (figures 13g,h) we again see a reversal of the sign of the onshore wind component and a reduction of θ_v, as expected from the vertical cross-sections in the model (figure 7). The forecast (figure 13h) has a fairly gradual decline in θ_v (around 2.3 K in 6 hours), which may be explained by the 2.2 km grid spacing not being fine enough to resolve the structure of the front. However, the observations (figure 13g) also show a more gradual transition to lower-θ_v air than is observed in other cases. The observed rainfall in this case is even lighter than in the lightest of the other six case studies, peaking at around 0.5 mm hr^{-1}, while the forecast peaks at around 12 mm hr^{-1} during the time of the front. (The earlier peak, at around 21 LT, is due to an unrelated, small but intense convective cell which appears before the land breeze propagation arrives.) As explained above, the fact that we are dealing with point data may explain this discrepancy, so this does not necessarily point to a bias in the forecast rainfall.

Also notable is the variability in the timing of the land breeze front. In the cases shown, this varies from around 17 LT to around 01 LT. This is likely to be related to the environmental wind, but an investigation of the causes of this variability is beyond the scope of this paper.

4. Discussion and conclusions

The offshore propagation of convection overnight from islands in the Maritime Continent is a key feature of the diurnal cycle in the region. However, the existing literature (see section 1) offers no strong consensus on the physical mechanisms behind this propagation. Understanding

the dynamics of intense precipitating storms is crucial for accurate forecasting and issuing early warnings of high-impact weather.

The most commonly proposed mechanisms are the triggering of convection progressively offshore due to low-level convergence between environmental onshore winds and offshore-propagating density currents (either due to the land breeze or cold pools); or the triggering of precipitation by gravity waves. Some studies suggest that gravity waves trigger convection directly; while others suggest they destabilize the atmosphere ahead of the convection but a further trigger is still required for the offshore convection to occur. A further contribution to the offshore propagation may arise from signals propagating from the other side of the island (seen propagating from right to left in the top-right corner of figure 2b), although these are beyond the scope of the present study, which focuses on orographic and coastal processes. The diurnal cycle is often studied in composites over many days, which may hide day-to-day variability in the timing, speed or direction of the propagation; and may appear to show propagation through averaging over what are in fact stationary or near-stationary precipitation features occurring on different days.

In this study we use a convection-permitting model and choose three case studies of offshore propagation observed during the JAMSTEC pre-YMC field campaign in November and December 2015, to examine the physical processes involved. These cases all had a prevailing wind in the offshore direction, and distinct offshore-propagating rainfall during the evening and overnight. The model grid spacing was 2 km and diagnostics were output every 5 minutes, which is sufficient to identify gravity waves and the gust front of a density current.

The results are summarized by the schematic diagram in figure 14. This shows a slice through Sumatra, as in figure 7, with the horizontal axis being approximately south-west (on the left) to north-east (on the right), the green peak being the Barisan mountains. The large grey arrow on the right indicates the prevailing wind direction. Black arrows are density currents within the planetary boundary layer; pink arrows represent gravity waves; and blue pointed lines are cold fronts, the points indicating the direction of propagation. The colour of the sky indicates day (light blue), evening (dark blue) or night (black). Note that the vertical heights, which are non-linear, and the timings shown in this diagram are representative only, as they may vary from day to day.

Insolation warms the land surface during the day, causing an onshore sea breeze density current. In reality the land surface warms and cools faster than the sea surface, meaning the land-sea

temperature contrast is warmer over the land during the day and warmer over the sea during the night. In our model the SST is fixed during the day, but the warming and cooling of the land still mean that the temperature contrast has the correct sign by day and by night. In a model with a diurnal cycle of SST, there would likely be a second-order impact on the speed and intensity of the land-sea breeze circulation and associated convection.

The sea breeze, whose front is indicated as a cold front on the diagram, propagates inland and up the slopes of the Barisan mountains (figure 14a). There is a corresponding upslope wind on the onshore side of the ridge causing convergence and ascent over the peaks; and some ascent due to low-level heating from the ground. Clouds form over the mountains and begin to precipitate (figure 14b).

The mountain-top convection deepens to form cumulonimbus storm clouds, typically by early-to-mid evening (figure 14c). Since this occurs along the mountain range, the deep convection is typically organized into a squall line, oriented along the direction of the mountains (which is also the direction of the coast). The convection triggers gravity waves which may propagate in all directions and their signals may be seen in the model at almost any altitude in the troposphere. In the schematic diagram we summarize this by drawing a single wave, propagating offshore at around 2 km altitude and with a phase speed of around 16 m s^{-1}, consistent with the $n = 3$ mode.

Once the land surface has cooled sufficiently to reverse the sign of the land-sea temperature contrast (figure 14d), a downslope density current appears. At first, katabatic flow occurs down the mountain, reinforced by the temperature contrast to form a land breeze density current which propagates offshore. The squall line also causes cold pools – regions of cold air due to evaporation, melting and sublimation of falling hydrometeors, which sink to due their high density and spread out upon hitting the surface, again creating a density current. Although in general it is possible to identify cold pools in the model (e.g., by plotting the gradient of low-level θ_v to identify their associated fronts, as in figure 6), close to the coastline it is extremely difficult to disentangle these cold pools from the sea breeze. Therefore, the cold front shown in figures 14d,e is assumed to be the net result of the katabatic wind, land breeze and cold pools. In future work, we hope to distinguish between these through the use of tracers in further convection-permitting model runs.

The motion of this offshore density current coincides with the squall line propagating offshore. The convection and its precipitation are always collocated with the low-level convergence between

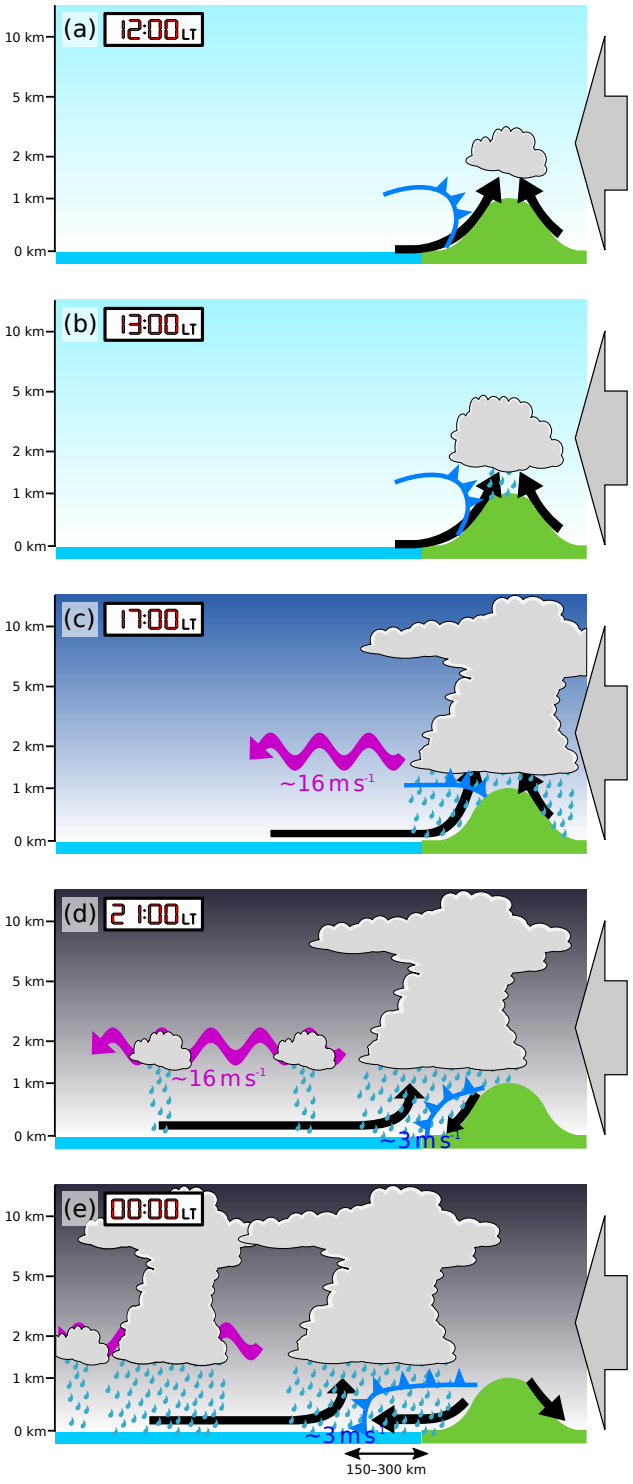

FIG. 14: Schematic diagram showing a day with an offshore prevailing wind and nocturnal offshore propagation of convection. The large grey arrow shows the prevailing wind direction and black arrows indicate density currents. Pink sinusoidal arrows represent gravity waves. Blue pointed lines are cold fronts, caused here by boundary layer density currents. The heights on the vertical axis, the horizontal length scale and the local times on the clock are representative only. The timing of the convection and its propagation may vary by several hours from day to day.

the density current and the remnant of the sea breeze from earlier in the day, out to around 150–300 km offshore. In the model runs, the propagation of the squall line is at a speed on the order 3 m s^{-1}. This provides further evidence that the propagation cannot be directly caused by gravity waves as the speed is far too slow. Moreover, observations from the AWS on the *R/V* Mirai show a density current propagating through at the time of day indicated by the model, accompanied by precipitation, verifying the mechanism outlined here. Hence, the physical processes involved are more akin to the mechanism of Houze et al. (1981) than the gravity wave mechanism of Mapes et al. (2003b,a; see section 1 for details), even though gravity wave mechanisms are often thought of as responsible for the nocturnal offshore propagation in the Maritime Continent region (e.g., Love et al. 2011; Yokoi et al. 2017; Coppin and Bellon 2019a). However, our results are consistent with those studies which draw a distinction between slower propagation near to the coast, associated with propagation of low-level convergence; and faster propagation further offshore, associated with gravity waves (e.g., Vincent and Lane 2016; Bai et al. 2021; Fang and Du 2022).

Our results also show evidence of gravity waves playing a role in offshore convection. It was not possible to establish any evidence for the waves destabilizing the atmosphere ahead of the propagation, as hypothesized by studies such as Love et al. (2011) and Hassim et al. (2016). Hovmöller diagrams of convective available potential energy, convective inhibition and moist static energy (not shown) did not show any signal specifically associated with the waves. However, a gravity wave may trigger convection which precipitates (e.g., Tulich and Mapes 2008), as indicated in the left-hand side of figure 14d, but it is generally weak and localized. However, if there is already an appreciable perturbation present, which the gravity wave interacts with, such as cloud caused by an earlier cold pool, it is possible for the gravity wave to trigger deep and intense convection there. This is indicated by the smaller cumulonimbus cloud in the left-hand side of figure 14e. Such events have previously been studied in observations and models. Marsham and Parker (2006) described a case study of a convective storm over southern England with three storms subsequently triggered nearby, with gravity waves being the likely cause. Birch et al. (2013) showed that an earlier version of the MetUM was able to reproduce observed secondary initiation of convection over continental west Africa, due to gravity waves interacting with pre-existing dry convection and an elevated boundary layer top.

Because the diurnal cycle over the Maritime Continent varies considerably from day to day, and the offshore propagation is not always as distinct as in the case studies chosen here, it is common to investigate the diurnal cycle in a composite sense (e.g., Peatman et al. 2014). As was demonstrated in figure 2, this can give the impression of a coherent envelope of precipitation propagating offshore over a range of speeds. The evidence of this study shows that the propagation at the slower speed can indeed be coherent, due to the organization of the convection that propagates along with the offshore density current. However, the gravity waves, which propagate at approximately the speed of the faster edge of the composite envelope, mainly trigger isolated rainfall in our case studies. Computing a composite may average over these isolated regions of rainfall, giving the appearance of a propagating signal at the same phase speed as the wave, even though the individual precipitation features causing it do not necessarily propagate at all, or may propagate slowly. This precipitation happens much further offshore than the propagating organized squall line.

The distinction between the day-to-day propagation and the apparent propagation in a composite is not necessarily important for climate studies, for example where we are interested in mean cloud cover and albedo forcing. In this case, the average gravity wave interactions with pre-existing convection are important in a climatological sense. However, in numerical weather prediction, and specifically in quantitative precipitation forecasting, where it is necessary to forecast the location and timing of convection on a particular day, the distinction is crucial.

The present study focuses on three case studies in which the prevailing wind is offshore, and the propagation is both strong and coherent. This study furthers the existing literature by analyzing individual cases at the process level, but the limited number of cases is insufficient to resolve completely the lack of consensus in the literature regarding the underlying physical mechanisms of the propagation. Further research will examine these mechanisms statistically over a much larger number of cases. It should also be noted that there are comparable previous studies investigating convection triggered by density currents and gravity waves over land (e.g., Birch et al. 2013) but, in the case of the Maritime Continent, the convection's continued evolution is over ocean. The presence of the ocean boundary layer likely means that the dynamics of the storm later in its lifetime are quite different from those seen over land, and this is again a topic worthy of future investigation.

However, the present study demonstrates, in order to forecast the timing and location of rainfall skilfully, the necessity of forecasting the propagation of the nocturnal land breeze and

the low-level convergence it generates; and understanding the more limited role of gravity waves in the distribution of rainfall.

Acknowledgments. This research was funded by the Met Office Weather and Climate Science for Service Partnership (WCSSP) Southeast Asia, as part of the Newton Fund; and the TerraMaris project, funded by National Environment Research Council (NERC) Grant NE/R016739/1. The field campaign data were collected as part of YMC, led by investigator Dr Kunio Yoneyama. The authors would like to thank Dr Joshua Hampton for assistance in reading radar data. This work used the ARCHER UK National Supercomputing Service (http://www.archer.ac.uk). Data analysis and plots used the Iris Python package for Earth science data, version 3.1.0 (Met Office 2021). We thank three anonymous reviewers for their comments and suggestions which improved the final manuscript.

Data availability statement. Himawari data are provided by the Japan Meteorological Agency; we thank the ICARE Data and Services Center (`http://www.icare.univ-lille1.fr/extract/subset/order`) for providing access to the Himawari data used in this study. IMERG data are provided by the National Aeronautics and Space Administration (NASA) Goddard Space Flight Center's Earth Science Division and Precipitation Processing System, which develop and compute the IMERG as a contribution to GPM; and archived at the NASA Goddard Earth Sciences Data and Information Services Center (GES DISC; `https://pmm.nasa.gov/data-access/downloads/gpm`). GLOBE data are provided by the National Oceanic and Atmospheric Administration (`https://www.ngdc.noaa.gov/mgg/topo/globe.html`). Radar and AWS data from the *R/V* Mirai are provided by the Japan Agency for Marine-Earth Science and Technology (JAMSTEC; `https://www.jamstec.go.jp/ymc/obs/pre-YMC/Mirai/index.html`).

APPENDIX

Identification of the direction of offshore propagation

Here we detail the algorithm for diagnosing the direction of offshore propagation on an individual day (if propagation can be identified). This algorithm was used to create figure 2b.

The gridded precipitation data over 36 hours, from 07 LT one day to 19 LT the next, are interpolated to a rotated transect such as the one in figure 1a, trying every integer number of

degrees of orientation from 0° (propagation due west) to 90° (propagation due south). The mean is computed over the width of the transect to produce a rotated Hovmöller diagram with dimensions of onshore distance (x) and time (t). An example is shown in figure A1a, for 2015/11/21 and an angle of 69°.

For each direction, the Hovmöller diagram is converted to a binary field, indicating whether the precipitation rate exceeds a subjectively-chosen threshold of 1 mm hr^{-1} (figure A1b), and contiguous features are identified. For propagation to exist, a precipitation feature must exist in the centre of the x-direction of this field (the equivalent of 102.05°N, 3.55°S – on the coast near Bengkulu) between 12 LT and 00 LT. If there are multiple such features, the only largest is retained (figure A1c).

The speed of propagation is then found by linear regression through points where $x < 0$ (i.e., over the sea) only. For each time from local noon until the feature disappears, all well-separated local maxima in precipitation rate are found and the maximum closest to the coast is retained. Linear regression is performed through the maxima that were chosen for each time, using the Theil-Sen method (Sen 1968; Conover 1980), which chooses the median line through all possible pairs of points. The gradient of this regression line gives us a speed associated with this transect angle (figure A1c).

The angle which maximizes the speed is chosen as the direction of propagation. In general, not all angles will give rise to a precipitation feature in the correct part of the Hovmöller diagram. If there is no such feature at any angle, that day is deemed to have no propagation. By this measure, propagation occurred on 1,254 days (used in the composite in figure 2b), or 33%, of the 3,806 days in figure 2a.

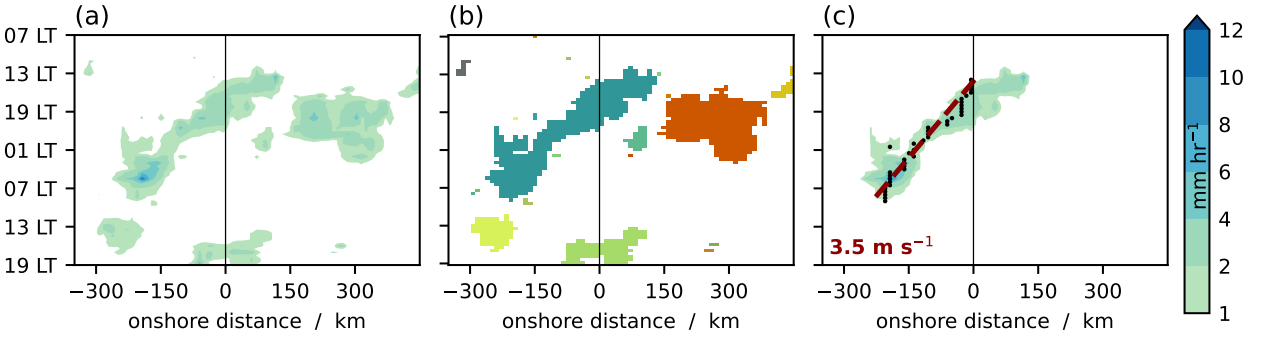

FIG. A1: Example of finding the offshore propagation speed for a Hovmöller diagram of precipitation rate at a given angle. (a) Hovmöller diagram of precipitation rate from IMERG for 2015/11/21 at an angle of 69°. (b) Contiguous features identified in a binary field of grid points where precipitation rate exceeds 1 mm hr^{-1}, coloured randomly. (c) Picking out only the contiguous feature which exists at the coast during local afternoon or evening (12 LT to 00 LT), a linear regression line is drawn (red dashed) through the local maximum at each time from 12 LT onwards. See appendix for full details.

References

Bai, H., and Coauthors, 2021: Formation of Nocturnal Offshore Rainfall near the West Coast of Sumatra: Land Breeze or Gravity Wave? *Monthly Weather Review*, **149 (3)**, 715–731, https://doi.org/10.1175/MWR-D-20-0179.1.

Bhatt, B. C., S. Sobolowski, and A. Higuchi, 2016: Simulation of diurnal rainfall variability over the Maritime Continent with a high-resolution regional climate model. *Journal of the Meteorological Society of Japan. Ser. II*, **94A**, 89–103, https://doi.org/10.2151/jmsj.2015-052.

Birch, C. E., D. J. Parker, A. O'Leary, J. H. Marsham, C. M. Taylor, P. P. Harris, and G. M. S. Lister, 2013: Impact of soil moisture and convectively generated waves on the initiation of a West African mesoscale convective system. *Quarterly Journal of the Royal Meteorological Society*, **139 (676)**, 1712–1730, https://doi.org/10.1002/qj.2062.

Bush, M., and Coauthors, 2020: The first Met Office Unified Model-JULES Regional Atmosphere and Land configuration, RAL1. *Geoscientific Model Development*, **13 (4)**, 1999–2029, https://doi.org/10.5194/gmd-13-1999-2020.

Conover, W. J., 1980: *Practical Nonparametric Statistics*. 2nd ed., John Wiley and Sons, New York, 511 pp.

Coppin, D., and G. Bellon, 2019a: Physical mechanisms controlling the offshore propagation of convection in the tropics: 1. Flat island. *Journal of Advances in Modeling Earth Systems*, **11**, 3042–3056, https://doi.org/10.1029/2019MS001793.

Coppin, D., and G. Bellon, 2019b: Physical mechanisms controlling the offshore propagation of convection in the tropics: 2. Influence of topography. *Journal of Advances in Modeling Earth Systems*, **11**, 3251–3264, https://doi.org/10.1029/2019MS001794.

Coppin, D., G. Bellon, A. Pletzer, and C. Scott, 2020: Detecting and Tracking Coastal Precipitation in the Tropics: Methods and Insights into Multiscale Variability of Tropical Precipitation. *Journal of Climate*, **33 (15)**, 6689–6705, https://doi.org/10.1175/JCLI-D-19-0321.1.

Dipankar, A., S. Webster, X.-Y. Huang, and V. Q. Doan, 2019: Understanding biases in simulating the diurnal cycle of convection over the western coast of Sumatra: comparison with pre-YMC observation campaign. *Monthly Weather Review*, **147 (5)**, 1615–1631, https://doi.org/10.1175/MWR-D-18-0432.1.

Duchon, C. E., 1979: Lanczos Filtering in One and Two Dimensions. *Journal of Applied Meteorology*, **18 (8)**, 1016–1022, https://doi.org/10.1175/1520-0450(1979)018<1016:LFIOAT>2.0.CO;2.

Fang, J., and Y. Du, 2022: A global survey of diurnal offshore propagation of rainfall. *Nature Communications*, **13 (1)**, 7437, https://doi.org/10.1038/s41467-022-34842-0.

GDAL/OGR contributors, 2022: GDAL/OGR geospatial data abstraction software library. URL https://gdal.org, https://doi.org/10.5281/zenodo.5884351.

Hassim, M. E. E., T. P. Lane, and W. W. Grabowski, 2016: The diurnal cycle of rainfall over New Guinea in convection-permitting WRF simulations. *Atmospheric Chemistry and Physics*, **16 (1)**, 161–175, https://doi.org/10.5194/acp-16-161-2016.

Hastings, D. A., and P. K. Dunbar, 1998: Development & Assessment of the Global Land One-km Base Elevation Digital Elevation Model (GLOBE). *International Society of Photogrammetry and Remote Sensing*, **32 (4)**, 218–221.

Hastings, D. A., and Coauthors, 1999: The Global Land One-kilometer Base Elevation (GLOBE) digital elevation model, version 1.0. URL http://www.ngdc.noaa.gov/mgg/topo/globe.html.

693 Houze, R. A., S. G. Geotis, F. D. Marks, and A. K. West, 1981: Winter monsoon convection in
694 the vicinity of north Borneo. Part I: Structure and time variation of the clouds and precipitation.
695 *Monthly Weather Review*, **109 (8)**, 1595–1614, https://doi.org/10.1175/1520-0493(1981)
696 109<1595:WMCITV>2.0.CO;2.

697 Huffman, G. J., E. F. Stocker, D. T. Bolvin, E. J. Nelkin, and J. Tan, 2019: GPM IMERG
698 Final Precipitation L3 Half Hourly 0.1 degree x 0.1 degree V06. https://doi.org/10.5067/GPM/
699 IMERG/3B-HH/06.

700 Jin, F., and B. J. Hoskins, 1995: The Direct Response to Tropical Heating in a Baroclinic
701 Atmosphere. *Journal of the Atmospheric Sciences*, **52 (3)**, 307–319, https://doi.org/10.1175/
702 1520-0469(1995)052<0307:TDRTTH>2.0.CO;2.

703 Lane, T. P., and M. J. Reeder, 2001: Convectively generated gravity waves and their effect on the
704 cloud environment. *Journal of the Atmospheric Sciences*, **58 (16)**, 2427–2440, https://doi.org/10.
705 1175/1520-0469(2001)058<2427:CGGWAT>2.0.CO;2.

706 Love, B. S., A. J. Matthews, and G. M. S. Lister, 2011: The diurnal cycle of precipitation over
707 the Maritime Continent in a high-resolution atmospheric model. *Quarterly Journal of the Royal*
708 *Meteorological Society*, **137**, 934–947, https://doi.org/10.1002/qj.809.

709 Mapes, B. E., T. T. Warner, and M. Xu, 2003a: Diurnal patterns of rainfall in northwestern South
710 America. Part III: Diurnal gravity waves and nocturnal convection offshore. *Monthly Weather*
711 *Review*, **131 (5)**, 830–844, https://doi.org/10.1175/1520-0493(2003)131<0830:DPORIN>2.0.
712 CO;2.

713 Mapes, B. E., T. T. Warner, M. Xu, and A. J. Negri, 2003b: Diurnal patterns of rainfall in
714 northwestern South America. Part I: Observations and context. *Monthly Weather Review*, **131 (5)**,
715 799–812, https://doi.org/10.1175/1520-0493(2003)131<0799:DPORIN>2.0.CO;2.

716 Marshall, J. S., and W. M. K. Palmer, 1948: The distribution of raindrops with size. *Journal of*
717 *Meteorology*, **5 (4)**, 165–166, https://doi.org/10.1175/1520-0469(1948)005<0165:TDORWS>
718 2.0.CO;2.

719 Marsham, J. H., and D. J. Parker, 2006: Secondary initiation of multiple bands of cumulonimbus
720 over southern Britain. II: Dynamics of secondary initiation. *Quarterly Journal of the Royal*
721 *Meteorological Society*, **132 (617)**, 1053–1072, https://doi.org/10.1256/qj.05.152.

722 Marzuki, M., H. Yusnaini, F. Tangang, R. Muharsyah, M. Vonnisa, and H. Harmadi, 2022: Land -
723 sea contrast of diurnal cycle characteristics and rain event propagations over Sumatra according
724 to different rain duration and seasons. *Atmospheric Research*, **270**, 106 051, https://doi.org/10.
725 1016/j.atmosres.2022.106051.

726 Met Office, 2021: Iris: A Python library for analysing and visualising meteorological and
727 oceanographic data sets. *http://scitools.org.uk*.

728 Mori, S., H. Jun-Ichi, Y. I. Tauhid, and M. D. Yamanaka, 2004: Diurnal land-sea rainfall
729 peak migration over Sumatera Island, Indonesian Maritime Continent, observed by TRMM
730 satellite and intensive rawinsonde soundings. *Monthly Weather Review*, **132 (8)**, 2021–2039,
731 https://doi.org/10.1175/1520-0493(2004)132<2021:DLRPMO>2.0.CO;2.

732 Peatman, S. C., A. J. Matthews, and D. P. Stevens, 2014: Propagation of the Madden-Julian
733 Oscillation through the Maritime Continent and scale interaction with the diurnal cycle of
734 precipitation. *Quarterly Journal of the Royal Meteorological Society*, **140 (680)**, 814–825,
735 https://doi.org/10.1002/qj.2161.

736 Peatman, S. C., J. Methven, and S. J. Woolnough, 2018: Isolating the effects of moisture
737 entrainment on convectively-coupled equatorial waves in an aquaplanet GCM. *Journal of the*
738 *Atmospheric Sciences*, **75 (9)**, 3139–3157, https://doi.org/10.1175/JAS-D-18-0098.1.

739 Peatman, S. C., J. Schwendike, C. E. Birch, J. H. Marsham, A. J. Matthews, and G.-Y. Yang,
740 2021: A Local-to-Large Scale View of Maritime Continent Rainfall: Control by ENSO,
741 MJO, and Equatorial Waves. *Journal of Climate*, **34 (22)**, 8933–8953, https://doi.org/10.1175/
742 JCLI-D-21-0263.1.

743 Qian, T., C. C. Epifanio, and F. Zhang, 2012: Topographic Effects on the Tropical Land and
744 Sea Breeze. *Journal of the Atmospheric Sciences*, **69 (1)**, 130–149, https://doi.org/10.1175/
745 JAS-D-11-011.1.

Ramage, C. S., 1968: Role of a Tropical "Maritime Continent" in the atmospheric circulation. *Monthly Weather Review*, **96 (6)**, 365–370, https://doi.org/10.1175/1520-0493(1968)096<0365:ROATMC>2.0.CO;2.

Sen, P. K., 1968: Estimates of the Regression Coefficient Based on Kendall's Tau. *Journal of the American Statistical Association*, **63 (324)**, 1379–1389, https://doi.org/10.1080/01621459.1968.10480934.

Tulich, S. N., and B. E. Mapes, 2008: Multiscale Convective Wave Disturbances in the Tropics: Insights from a Two-Dimensional Cloud-Resolving Model. *Journal of the Atmospheric Sciences*, **65 (1)**, 140–155, https://doi.org/10.1175/2007JAS2353.1.

Vincent, C. L., and T. P. Lane, 2016: Evolution of the diurnal precipitation cycle with the passage of a Madden-Julian Oscillation event through the Maritime Continent. *Monthly Weather Review*, **144 (5)**, 1983–2005, https://doi.org/10.1175/MWR-D-15-0326.1.

Vincent, C. L., and T. P. Lane, 2017: A 10-year austral summer climatology of observed and modeled intraseasonal, mesoscale, and diurnal variations over the Maritime Continent. *Journal of Climate*, **30 (10)**, 3807–3828, https://doi.org/10.1175/JCLI-D-16-0688.1.

Wheeler, M. C., and H. H. Hendon, 2004: An all-season real-time multivariate MJO index: Development of an index for monitoring and prediction. *Monthly Weather Review*, **132**, 1917–1932, https://doi.org/10.1175/1520-0493(2004)132<1917:AARMMI>2.0.CO;2.

Wheeler, M. C., and G. N. Kiladis, 1999: Convectively Coupled Equatorial Waves: Analysis of Clouds and Temperature in the Wavenumber-Frequency Domain. *Journal of the Atmospheric Sciences*, **56 (3)**, 374–399, https://doi.org/10.1175/1520-0469(1999)056<0374:CCEWAO>2.0.CO;2.

Wu, P., M. Hara, J.-i. Hamada, M. D. Yamanaka, and F. Kimura, 2009: Why a large amount of rain falls over the sea in the vicinity of western Sumatra Island during nighttime. *Journal of Applied Meteorology and Climatology*, **48 (7)**, 1345–1361, https://doi.org/10.1175/2009JAMC2052.1.

Yokoi, S., S. Mori, F. Syamsudin, U. Haryoko, and B. Geng, 2019: Environmental conditions for nighttime offshore migration of precipitation area as revealed by in situ observation

off Sumatra Island. *Monthly Weather Review*, **147 (9)**, 3391–3407, https://doi.org/10.1175/MWR-D-18-0412.1.

Yokoi, S., Y. Nakayama, Y. Agata, T. Satomura, K. Kuraji, and J. Matsumoto, 2012: The relationship between observation intervals and errors in radar rainfall estimation over the Indochina Peninsula. *Hydrological Processes*, **26 (6)**, 834–842, https://doi.org/10.1002/hyp.8297.

Yokoi, S., and Coauthors, 2017: Diurnal cycle of precipitation observed in the western coastal area of Sumatra Island: offshore preconditioning by gravity waves. *Monthly Weather Review*, **145 (9)**, 3745–3761, https://doi.org/10.1175/MWR-D-16-0468.1.

Yoneyama, K., and C. Zhang, 2020: Years of the Maritime Continent. *Geophysical Research Letters*, **47 (12)**, e2020GL087 182, https://doi.org/10.1029/2020GL087182.